No evidence of extraterrestrial noble metal and helium anomalies at Marinoan glacial termination

Bernhard Peucker-Ehrenbrink [a,*], Christine A. Waters [a,b], Mark D. Kurz [a] and Paul F. Hoffman [c]

[a] *Woods Hole Oceanographic Institution, Department of Marine Chemistry and Geochemistry, Woods Hole, MA 02543, U.S.A.*

[b] *University of Texas at El Paso (UTEP), El Paso, TX 79902, now at: University of Hawai'i at Mānoa (SOEST), Honolulu, HI 96822, U.S.A.*

[c] *Harvard University, Cambridge, MA 02138, U.S.A, now at: University of Victoria, BC, V8P 5C2, Canada.*

[*] Corresponding author. Tel.: +01 508 289 2518. *E-mail address*: behrenbrink@whoi.edu (B. Peucker-Ehrenbrink).

Keywords: snowball earth, osmium isotopes, iridium, helium isotopes, extraterrestrial matter, cap carbonate

ABSTRACT

High concentrations of extraterrestrial iridium have been reported in terminal Sturtian and Marinoan glacial marine sediments and are used to argue for long (likely 3-12 Myr) durations of these Cryogenian glaciations. Reanalysis of the Marinoan sedimentary rocks used in the original study, supplemented by sedimentary rocks from additional terminal Marinoan sections, however, does not confirm the initial report. New platinum group element concentrations, and $^{187}Os/^{188}Os$

and $^{3}He/^{4}He$ signatures are consistent with crustal origin and minimal extraterrestrial contributions. The discrepancy is likely caused by different sample masses used in the two studies, with this study being based on much larger samples that better capture the stochastic distribution of extraterrestrial particles in marine sediments. Strong enrichment of redox-sensitive elements, particularly rhenium, up-section in the basal postglacial cap carbonates, may indicate a return to more fully oxygenated seawater in the aftermath of the Marinoan snowball earth. Sections dominated by hydrogenous osmium indicate increasing submarine hydrothermal sources and/or continental inputs that are increasingly dominated by young mantle-derived rocks after deglaciation. Sedimentation rate estimates for the basal cap carbonates yield surprisingly slow rates of a few centimeters per thousand years. This study highlights the importance of using sedimentary rock samples that represent sufficiently large area-time products to properly sample extraterrestrial particles representatively, and demonstrates the value of using multiple tracers of extraterrestrial matter.

1. Introduction

The most extreme and prolonged ice ages of the past two billion years were the Sturtian (717 to 660 Ma) and Marinoan (~645 to 635 Ma) panglacial epochs of the Cryogenian period (Gradstein et al. 2012), when ice sheets flowed into the ocean close to the paleomagnetic equator (Harland, 1964; Embleton and Williams, 1986; Schmidt et al., 1991; Sohl et al., 1999; Evans, 2000, 2003; Macdonald et al., 2010; Evans and Raub, 2011). High orbital obliquity (Williams, 1975) and albedo instability associated with large ice caps (Kirschvink, 1992) are among the proposed explanations for Cryogenian glaciations. High orbital obliquity causes the Hadley cells to reverse direction (i.e., equatorial downwelling), shifting the arid zones to the equator. This prediction is not borne out by persistent subtropical paleomagnetic latitudes for evaporite

deposits over the past two billion years (Evans, 2006), assuming that obliquity cannot flip between low and high values (Laskar et al., 1993). Moreover, mid-latitude sea-ice margins are unstable under high obliquity (Ferreira et al., 2014). A stable atmospheric inversion in the winter hemisphere creates a surface layer of calm air, which paralyzes wind-driven ocean mixing at the sea-ice margin and thereby reduces the ocean heat capacity, facilitating winter sea-ice advance. These considerations limit the apparent climatic scenarios that are consistent with tropical ice sheets on the continents to three possibilities (Rodehacke et al., 2013): (1) 'Snowball', in which the sea-ice margins meet at the equator and thicken to form dynamic sea glaciers (Warren et al., 2002; Goodman and Pierrehumbert, 2003; Li and Pierrehumbert, 2011; Abbot et al., 2013), with "some warm tropical 'puddles' in the sea of ice, shifting slightly from north to south with the seasons" (Kirschvink, 1992); (2) 'Jormungand', in which the sea-ice margins stabilize between 12 and 24 degrees of latitude because of broadening of the ablative zone of dark sea ice when it intersects the downward limb of the Hadley cells (Abbot et al., 2011; Voigt and Abbot, 2012); and (3) 'Waterbelt', in which the sea-ice margins stabilize between 20 and 30 degrees of latitude because of intensified ocean mixing at the sea-ice margin as the width of open water narrows (Rose, 2015). In the Snowball state, extraterrestrial (ET) matter should be trapped by the sea glacier and advected to the ablation zone, where it accumulates at or near the ice surface until terminal deglaciation (Abbot and Pierrehumbert, 2010; Li and Pierrehumbert, 2011). In the Jormungand and Waterbelt states, in contrast, ET matter should be advected to the sea-ice margins, where it is continuously flushed into the ocean in the zone of most intense ocean mixing (Rose, 2015).

The report of significant iridium (Ir) anomalies – allegedly of extraterrestrial origin – coinciding with Sturtian and Marinoan glacial terminations created the prospect of using the

accumulation rate of ET matter as a chronometer for glacial durations (Bodiselitsch et al., 2005). Extraterrestrial matter is enriched in Ir ~10,000-fold compared to average eolian dust, upper continental (Kurat et al., 1994; Peucker-Ehrenbrink and Jahn, 2001) and oceanic (Peucker-Ehrenbrink et al., 2003, 2012) crusts. Iridium therefore serves as one of the most sensitive refractory tracers for the presence of ET matter in sediments. Concentrations of up to 1.9 ng/g Ir, similar in magnitude to many K-Pg boundaries (Cretaceous-Paleogene, e.g., Alvarez et al., 1980; Schulte et al., 2010), have been reported just above the base of the postglacial (cap) carbonates that overlie the youngest Sturtian (~660 Ma) and Marinoan (~635 Ma) glacial sediments of the Lufilian Arc in central Africa (Bodiselitsch et al., 2005). The Ir anomalies are apparently not associated with anomalies of elements enriched in the continental crust (e.g., Al, Fe, Th, Cs). Rather, they are coupled with unusual concentrations of other noble metals, specifically gold. This geochemical evidence has been used to argue for an ET pedigree of the Ir (Bodiselitsch et al., 2005).

Following the approach used by Alvarez et al. (1980) for determining sediment accumulation rates across the K-Pg boundary, based on a constant flux of small ET matter to Earth, Bodiselitsch et al. (2005) suggested that ET matter had accumulated on the Marinoan ice sheets and sea glaciers for at least 3, more likely 12 million years (Myr), depending on the assumed flux of ET matter to Earth (Love and Brownlee, 1993; Schmitz et al., 1997). The data and model assumptions permit an even longer duration of 41 ± 20 Myr. The ET material supposedly was stored for prolonged periods in the thick sea glaciers and ice sheets and quickly delivered to marine sediments during deglaciation. As both types of ice are in a dynamic state in a snowball earth (Pierrehumbert et al., 2011), the global ice residence time is much less than the duration of the snowball epoch. However, unlike the Jormungand or Waterbelt climate states, in a snowball

92 earth, ET material entrained in sea glaciers remained in the ice and accumulated over time in the
93 equatorial ice ablation zone (Abbot and Pierrehumbert, 2010), because the meteoric fraction of
94 the sea glacier only sublimates, while only the marine (freeze-on) ice undergoes basal melting
95 (Li and Pierrehumbert, 2011). Some leakage of ET material stored in all meteoric ice sheets will
96 occur through basal melting and drainage of meltwater into the ocean at ice grounding lines.
97 However, in a snowball earth climate state the global ice volume is dominated by sea glaciers
98 that entrain ET material, not by ice sheets.

99 In this study we use the coherent geochemical properties of platinum group elements (PGE:
100 palladium, iridium, osmium, platinum), in conjunction with rhenium-osmium isotope
101 systematics, to test the presence and origin of the purported extraterrestrial Ir anomalies in a
102 number of Cryogenian glacial terminations, including some of the same samples analyzed by
103 Bodiselitsch et al. (2005). In contrast to the Bodiselitsch et al. (2005) study, we sampled critical
104 intervals continuously and homogenized "strips" of sedimentary rock to obtain continuous
105 geochemical records. In searches for geochemical anomalies, this approach ensures that no
106 major anomalies – if present – will be missed. As long as extraterrestrial contributions in
107 sedimentary rocks can be quantified, a global inventory can be calculated by integrating over
108 many sites with variable ET accumulation rates. Such an approach, akin to estimates of global
109 PGE inventories across the K-Pg boundary (Tredoux et al., 1989; Goderis et al., 2013), could be
110 used to estimate the flux of ET matter deposited across the glacial-postglacial transition.

111 In addition to the PGE, we tested the use of helium (He) isotopes and concentrations as an
112 additional tracer for the presence of ET matter in the sediments studied. The large contrast in
113 isotope ratios and concentrations of He in ET matter and Earth's crust makes He an even more
114 sensitive tracer for the presence of ET matter in sediments than Os isotopes and PGE abundance

pattern. Moreover, in a study of Ordovician limestones in south central Sweden, Patterson et al. (1998) have shown that some extraterrestrial He can survive protracted storage in sedimentary rocks as old as – and possibly older than – 480 Myr, despite its inherent volatility.

2. Samples and Sampling Procedures

Sections of sedimentary rocks spanning the Marinoan glacial-postglacial transition from a variety of depositional environments along the shelf-slope transition of the Otavi platform, Namibia (Hoffman et al., 1998, 2007; Hoffman and Halverson, 2008; Hoffman, 2011), were cut with a portable, petrol-powered, air-cooled Stihl TS 400 Cutquik circular saw equipped with a new diamond saw blade (Fig. 1a-c). In this area of central and northern Namibia, the glacial Ghaub Formation underlies the postglacial Maieberg cap carbonates. A total of five sedimentary sections were sampled from a variety of outcrops of the diamictite-cap dolomite transition. The results from two such sections are reported here (section P6538 [for map and section see Fig. 12 of Hoffman, 2005], 1 km North of Fransfontein, East of the road: 20°11.970' S, 015°00.987' E, 1150 m above mean sea level [m.a.s.l.]; and Hoanib River valley: 19°19.116' S, 013°59.481' E, 895 m.a.s.l.)

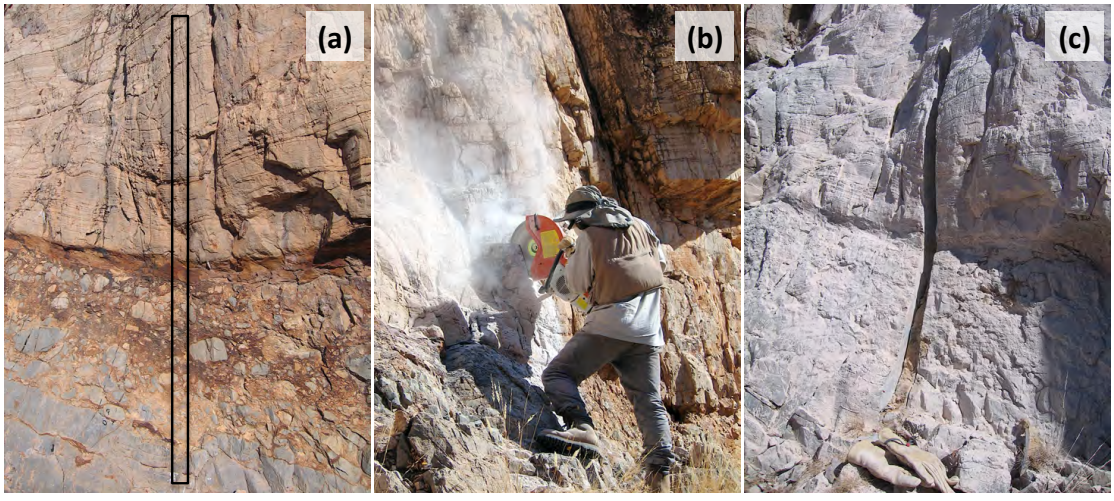

131 **Figure 1 (a)** Pre-glacial Ombaatjie Formation (bottom), Ghaub (Marinoan) glacial diamictite
132 (above), boundary clay (center) to post-glacial cap carbonate (top) transition on the Otavi
133 platform in NW Namibia, section 081105.04 – before cutting, with approximate position of the
134 section (black rectangle); **(b)** during cutting; **(c)** after chiseling of the section from the cut trench.

135 Two parallel cuts about 5 cm apart and about 14 cm deep were made across the transitions (Fig.
136 1b,c). The sections were marked, photographed, then extracted with chisel and hammer,
137 photographed again and bagged for transport to the laboratory (Fig 1a-c). There, strips of ~3 cm
138 width and 5-10 cm length were cut from these sections with a diamond saw blade. The outsides
139 of the strips were washed, cleaned with Al_2O_3 powder in a sandblaster to remove impurities from
140 the sawing, and then cleaned with pressurized air to remove Al_2O_3 beads. The strips were then
141 broken with a hammer between plastic bags, crushed in a jaw crusher equipped with tungsten
142 carbide plates, and pulverized in an Al-ceramic barrel in a shatter box. The equipment was
143 cleaned with silica powder between samples to avoid cross contamination, and preconditioned
144 with a small amount of sample material that was subsequently discarded.

145 Additional samples from NW Canada (transition from Stelfox diamictite into the overlying
146 Ravensthroat cap dolomite, Mackenzie Mountains, including continuous samples of the bottom 1
147 meter of the cap dolostone) and South China (transition from Nantuo diamictite into overlying
148 Doushantuo cap dolostone, Huajipo section, Yangtze Gorges area, Hubei Province, Fig. 2) were
149 obtained from the Harvard University collection and processed for analysis as described above.

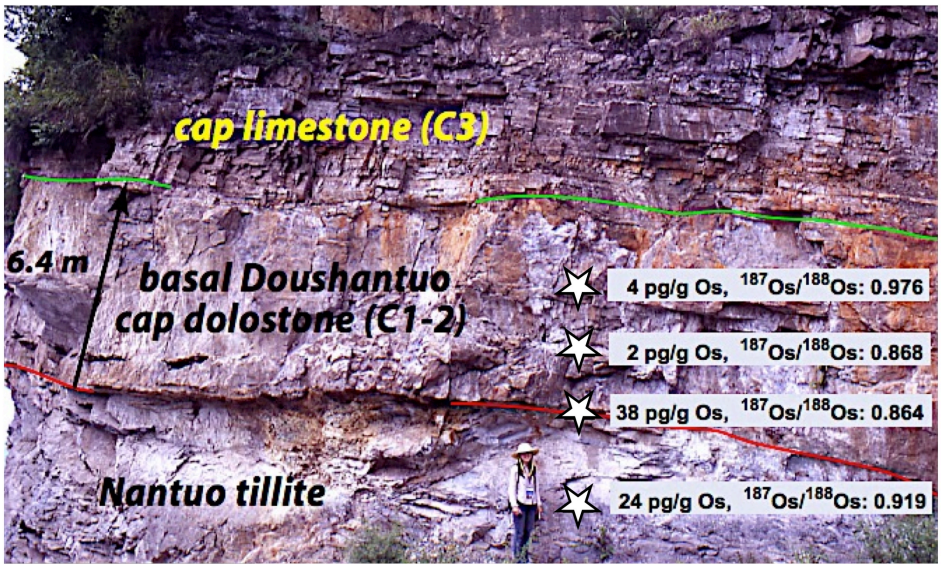

Figure 2 Nantuo tillite to basal Ediacaran cap dolostone (lower Doushantuo Formation) transition at the Huajipo section, Yangtze Gorges area, Hubei, South China, with osmium concentrations and $^{187}Os/^{188}Os$ values superimposed. Approximate sample locations are indicated by the white stars. Red line marks the boundary clay. Green line marks a 635 ± 0.5 Myr old volcanic ash (Condon et al., 2005). Person near bottom for scale. (Photo: P.F. Hoffman)

The samples from the Mackenzie Mountains include the continuous one meter interval of basal Ravensthroat cap dolomite from the Gayna River section (64°49'N, 130°28'W, 1855 m.a.s.l.; for map, schematic stratigraphy and field photo see Figs. 1 and 4b in Macdonald et al., 2013) that was complemented by a sample of the 2-12 cm thick underlying clay layer and several discrete samples of the underlying Stelfox diamictite that were taken from the Cranswick Lake section (65°06'N, 132°27'W, 1606 m.a.s.l.) and the Stone Knife River section (64°41'N, 129°53'W, 1596 m.a.s.l.) Sampling of the Ravensthroat cap dolomite at the Gayna River section was extended up to 4.3 meters above the base of the cap dolomite by discrete, non-continuous sampling. The total (not decompacted) thickness of the strata above the Ravensthroat formation

166 at the time of Cretaceous thrusting was 5.5 km (Gordey et al., 2010), and the strata was likely
167 thickened to ~8 km as a result of thrusting and before erosion. Assuming a geotherm of 25°C
168 km^{-1} yields prolonged temperatures of ~150°C before thrusting, and transient heating to <210°C
169 after thrusting is possible based on thermal maturation data for upper Devonian hydrocarbon-
170 bearing units near the top of the pre-thrust section (MacNaughton et al., 2008). Such prolonged
171 heating could have affected the integrity of the primary He budget of these rocks.

172 Marinoan syndeglacial cap dolostones like the Keilberg Member in NW Namibia,
173 Ravensthroat Formation in NW Canada and basal Doushantuo Formation in South China form
174 the transgressive tracts of exceptional depositional sequences associated with global ice-sheet
175 meltdown at the end-Cryogenian glacial termination (Kennedy, 1996; James et al., 2001;
176 Hoffman and Schrag, 2002; Shields, 2005; Hoffman et al., 2007; Bao et al., 2008). The
177 glacioeustatic component of the large-scale marine transgression was global and geologically
178 rapid (kyrs) because of positive feedbacks in the climate system (e.g., ice-albedo feedback, ice-
179 elevation feedback, GHG-temperature feedback, isostasy-outgassing feedback) and because most
180 Marinoan ice sheets were tropically located (Li et al., 2013). Marinoan cap dolostones have
181 $\delta^{13}C_{carb}$ profiles and an assortment of unusual sedimentary features that easily distinguish them
182 from older Cryogenian (Sturtian) postglacial cap carbonates (Kennedy et al., 1998; Hoffman et
183 al., 2011). The Marinoan cap dolostones in Namibia, NW Canada, South China and elsewhere
184 are easily recognizable and a product of global change, implying global synchronicity, which led
185 to the placement of the GSSP for the Ediacaran Period at its base (Knoll et al., 2006). The
186 validity of this stratigraphic assignment has been borne out by radiometric geochronology. U-Pb
187 zircon ID-TIMS dates of 635.2 ± 0.5 and 635.5 ± 0.8 Ma have been obtained from tuffs within
188 Marinoan cap dolostones in South China and Tasmania, respectively (Condon et al., 2005;

189 Calver et al., 2013), and tuffs in terminal Marinoan glacial deposits have been dated by the same
190 method at 635.5 ± 0.5 Ma in Namibia (Hoffmann et al., 2004). In NW Canada, a Re-Os isochron
191 age of 632.3 ± 5.9 Ma has been obtained from organic-rich black shale directly overlying the
192 Ravensthroat cap dolostone (Rooney et al., 2015).

193 ## 3. Experimental

194 ### *3.1. $^{187}Os/^{188}Os$ and PGE concentrations*

195 For PGE and $^{187}Os/^{188}Os$ analyses ~10 gram of sample powder was spiked with a mixed-PGE
196 tracer solution enriched in ^{99}Ru, ^{105}Pd, ^{190}Os, ^{191}Ir, and ^{198}Pt and processed according to
197 procedures described in detail in Ravizza and Pyle (1997) and Hassler et al. (2000). Osmium
198 isotopes were analyzed by distilling (sparging) volatile Os into a Thermo Fisher Neptune
199 inductively-coupled plasma mass spectrometer (ICPMS) equipped with multiple ion counters,
200 using data acquisition and data reduction routines described in detail in Sen and Peucker-
201 Ehrenbrink (2014). Concentrations of PGE were determined on a Thermo Finnigan Element2
202 ICPMS using the sparging solutions left after $^{187}Os/^{188}Os$ analyses (Hassler et al., 2000).
203 Whenever possible (Ru, Pd, Os, Pt), PGE concentrations were determined using at least two
204 isotope ratios that ideally yield concentrations that agree within analytical error. In cases when
205 the difference in concentration calculated by two isotope ratios is larger (≥19%), we chose to
206 report the lower concentration, as this minimizes the potential of concentrations being affected
207 by unrecognized interferences. The analytical methods for PGE concentrations and $^{187}Os/^{188}Os$
208 values have been carefully evaluated with international reference materials and in-house
209 standards (see Peucker-Ehrenbrink et al., 2003).

210 ### *3.2. Rhenium and Molybdenum concentrations*

211 Rhenium concentrations in all and molybdenum (Mo) concentrations in the Ravensthroat
212 sections were determined by isotope dilution (^{185}Re, ^{98}Mo) on ~100 mg aliquots of the same
213 sample powder after digestion in hot mineral acids, ion exchange chromatography and Element2
214 ICPMS data acquisition using methods described in detail in Miller et al. (2011). We emphasize
215 that Os and Re-Mo concentration data were generated using different splits of the same powder.
216 This procedure is not ideal for Re-Os isochron analyses, as nugget effects contribute to
217 variability in PGE concentrations. We therefore do not attempt to use Re-Os isochron
218 relationships to determine ages of any of the samples analyzed in this study. Results are
219 summarized in supplemental data table 1 (Table S1).

220 *3.3. ^{3}He/^{4}He and He concentrations*

221 Three contrasting samples from the Ravensthroat sections – a cap carbonate, a boundary
222 clay, and the matrix of a glacial diamictite – were prepared for He isotope analyses by manually
223 crushing and pulverizing pieces of rock in a stainless steel mortar and pestle that had been
224 cleaned first with acetone and then with isopropanol. Manual crushing avoids heating the
225 sample powder that is associated with mechanical grinding in planetary disc mills and thus
226 minimizes loss of helium during sample preparation. 8.25 grams of a cap dolomite sample (PI
227 0.05) were decarbonated in an isopropanol-cleaned Erlenmeyer flask with a mixture of 30 ml
228 ultra-clean (Millipore, ≥18.2 MΩ) water and up to 30 ml ~1.8 N acetic acid. The large sample
229 volume is needed to maximize the area-time product in order to minimize bias against larger ET
230 particles (Farley et al., 1997) in carbonate sediments of poorly constrained accumulation rates
231 (Hoffman and Schrag, 2002; Hoffman et al., 2007; Font et al., 2010). Dilute acetic acid is an
232 effective means for dissolving carbonate without affecting extraterrestrial He (Marcantonio et al.,
233 1999). The acetic acid was added stepwise to the water over several days, aided by repeated 15-

minute intervals of ultra-sonication. Finally, 2/3 of the supernatant was decanted and 6 ml of ~1.8 N acetic acid was added to test for additional degassing of CO_2 during ultra-sonication. After the reaction stopped, the solution was filtered through a pre-cleaned 0.45 μm silver filter, placing this filter into a filter holder of a vacuum filtration device. The Erlenmeyer flask was washed three times with 18.2 MΩ Millipore water followed by three washes with isopropanol. The sample was then air-dried in the vacuum pump for one hour before the Ag-filter was placed onto an isopropanol-washed thick Al-foil and wrapped tightly to avoid material escaping from the foil package. Two additional samples, ~0.85 g of a boundary clay (P5B -0.05) and ~1.5 grams of the fine-grained matrix of a glacial diamictite (P5B -0.30) were treated in a very similar manner. The only difference was that the samples were first suspended in 5 ml 18.2 MΩ Millipore water and 2.5 ml of ~1.8 N acetic acid was added stepwise, followed by repeated ultra-sonication. No degassing of CO_2 was observed during the treatment of these two clay-rich samples.

The tightly wrapped Al-foil packages were loaded into the ultra-high-vacuum sample extraction line of a helium isotope mass spectrometer. Once outgassing was reduced to an acceptable level, samples were dropped into a double vacuum resistance furnace and heated to 1600°C. The volatiles were introduced into a noble gas extraction line optimized for purification of He. Ion beam intensities of ^{3}He and ^{4}He were analyzed in a 90 degree sector mass spectrometer dedicated to helium, locally referred to as MS2 (Kurz et al., 2004). Total procedural blanks for ^{3}He and ^{4}He did not exceed 0.5% and 1%, respectively, of the lowest concentrations measured in the samples (cap dolostone P1-0.05) and typically were about 4 orders of magnitude smaller. We consider these contributions negligible. Results are summarized in supplemental data table 1 (Table S1).

3.4 Major and Trace Element concentrations

Major and trace element concentration of the Ravensthroat sections samples (Mackenzie Mountains, NW Territories, Canada) were determined in the SARM lab at the CRPG-CNRS at the University of Nancy, France. Major and some trace element concentrations were measured by ICP-AES on $LiBO_2$ fusions and complemented with additional trace element analyses by ICPMS. International reference materials were used to control data quality. The data and relevant metadata for all samples, analytical uncertainties and an international reference standard (USGS-SDO-1) are summarized in supplemental data table 1 (Table S1).

4. Results

4.1. Ravensthroat Sections

The carbonate-rich nature of most of this section is clearly visible in the high Ca and Mg concentrations and significantly elevated Mn concentrations relative to the continental crustal average (Fig. 3a,b). In order to evaluate trends in element concentrations across the section, we use an approach that first subtracts a local detrital component from the bulk and then normalizes the residual element concentrations to upper continental crustal (UCC) concentrations (McLennan, 2001).

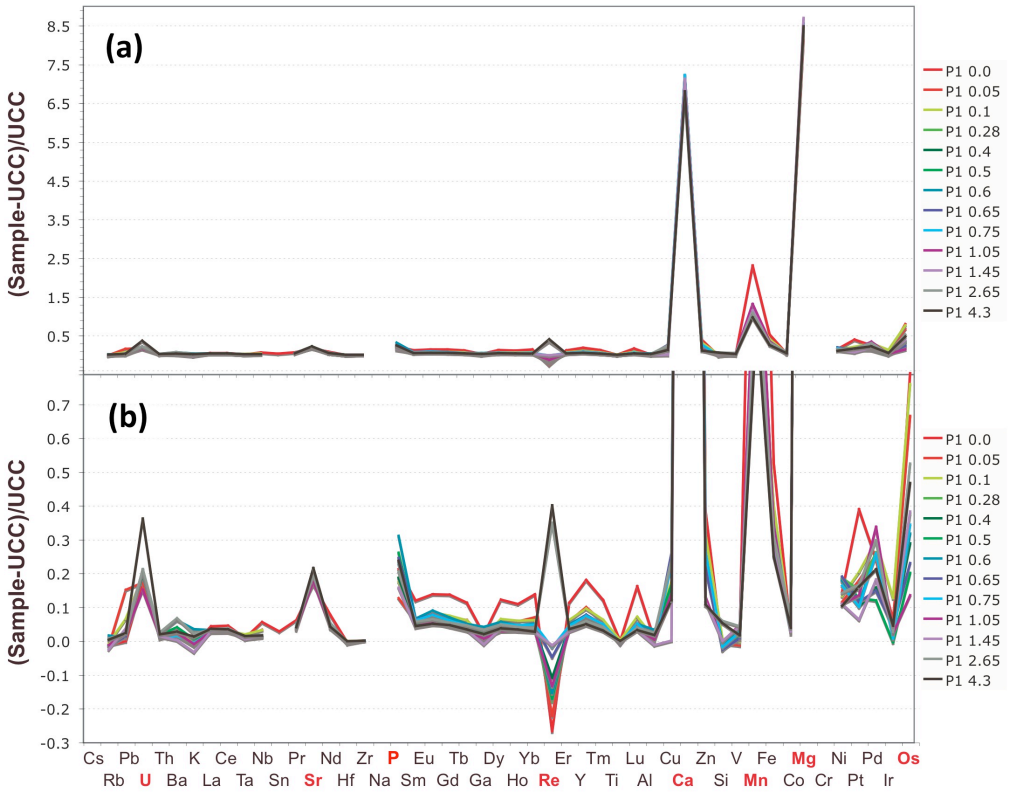

Figure 3 (**a**) Zirconium-normalized element enrichment/depletion relative to upper continental crust (McLennan, 2001) in cap carbonates from the Ravensthroat sections, Mackenzie Mountains, NW Canada. Elements are ordered from left to right in decreasing order of compatibility in the continental crust. Elements with notable anomalies are highlighted in red. Legends mark height (in m) of cap carbonate samples above the boundary clay. (**b**) Same as (a), but with an expanded scale.

If $[X]_i$ is the concentration of element X in sample i, and $[X]_{ref}$ is the concentration of the same element in the sample from the section that is most influenced by detrital matter, the residual concentration of element X in sample i, $[X]_{ir}$, normalized to UCC is calculated as:

$$[X]_{ir} = \{([X]_i - ([X]_{ref}\,[Zr]_i/[Zr]_{ref})) / [X]_{UCC}\}$$

Normalization to zirconium (Zr) can be replaced by normalizations to other "immobile" elements such as Al or Th (Hodson, 2002), but the choice of internal normalizing element has little effect

on the observed abundance pattern. We subtract a local detrital component because the sample that is most strongly influenced by detrital matter in this section, the boundary shale, has slightly higher Zr concentrations (225 µg/g) than average UCC (190 µg/g, McLennan, 2001). This ensures that residual concentrations, i.e. bulk minus the detrital component, are positive.

Uranium, strontium and phosphorus show minor enrichments in the non-detrital fraction relative to UCC, whereas Re and Os exhibit both enrichments and depletions depending on the position within the section and the choice of normalizing element (Fig. 3b). The section is characterized by a prominent spike in concentrations of PGE at the boundary between the cap dolostone and the underlying diamictites, with Ir concentrations exceeding 100 pg/g at the boundary (Figs. 3b, 4, top,bottom). Concentration differences between the two lithologic units range from almost two orders of magnitude in the case of Os and Re (Fig. 4b), to more than an order of magnitude for Ir (Fig. 4, top, bottom), to about one order of magnitude in the case of Pt and Pd (Fig. 4, bottom). The shapes of CI-chondrite normalized concentration pattern show little variation despite more than an order of magnitude variation in absolute concentrations (Fig. 4, bottom).

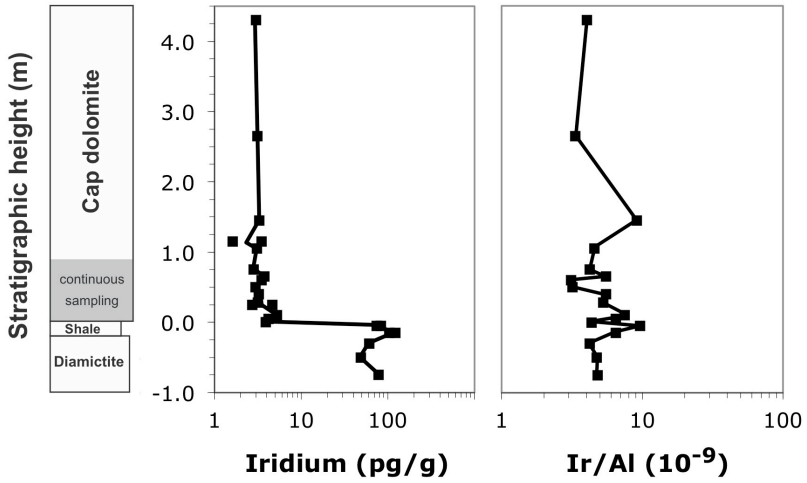

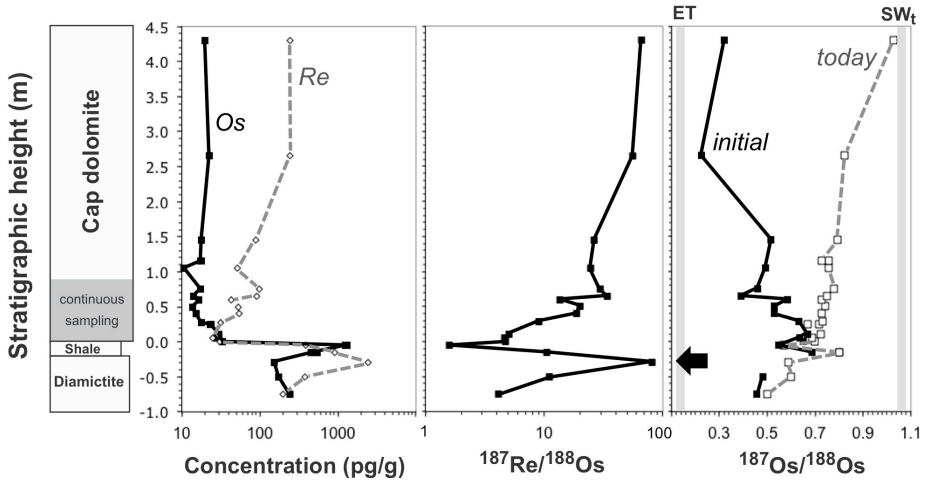

301

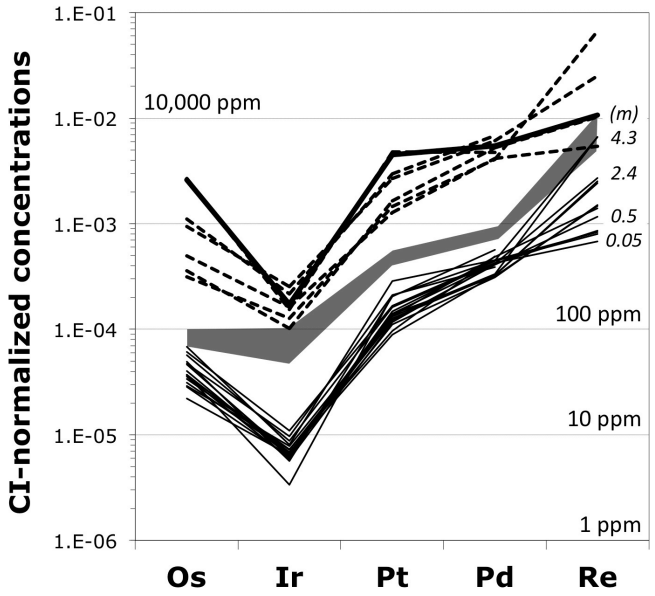

302

303 **Figure 4** (**top**) Iridium concentrations (left) and Ir/Al weight ratios (right) in the diamictite to
304 cap carbonate transition in the Ravensthroat sections, Mackenzie Mountains, NW Canada. Note
305 that only the first meter above the boundary clay has been sampled continuously. (**middle**)
306 Osmium and Re concentrations (left) $^{187}Re/^{188}Os$ (center) and present-day (gray line and white
307 squares) as well as initial (black line and squares) $^{187}Os/^{188}Os$ in the diamictite to cap carbonate
308 transition in the same section. (**bottom**) CI-normalized PGE concentrations in diamictite
309 (stippled lines), boundary clay (thick black line) and cap carbonate (thin black lines) in the same

section. Also shown are the distance of cap carbonate samples above the boundary clay (in m), and concentration of pure CI-chondrite matter in sediments (in parts per million, ppm). UCC composition is shown as gray field (Peucker-Ehrenbrink and Jahn, 2001, and references therein).

All samples are enriched in Os relative to Ir, and many, but not all, samples are also characterized by enrichments in Re (Fig. 4, bottom). While concentrations of PGE do not change significantly above 0.5 m from the boundary shale, Re concentrations increase up-section by almost an order of magnitude (Fig. 4, bottom). Correspondingly, $^{187}Re/^{188}Os$ vary by more than one order of magnitude from the boundary shale to the top of the section (Fig. 4b). Ingrowth-corrected $^{187}Os/^{188}Os$ values vary little across the lithologic transitions, but tend to become less radiogenic (~0.6 to ~0.25) in the overlying cap dolostone away from the boundary (Fig. 4, middle). Interestingly, concentrations of some redox-sensitive elements (U, Re) in the calculated detrital-free sediment fraction systematically increase from the base of the cap dolostone to the top of the section (Figs. 3a,b, 4b). Helium isotope ratios and concentrations in the three samples analyzed (Fig. 5) are typical of UCC (Marcantonio et al., 1998).

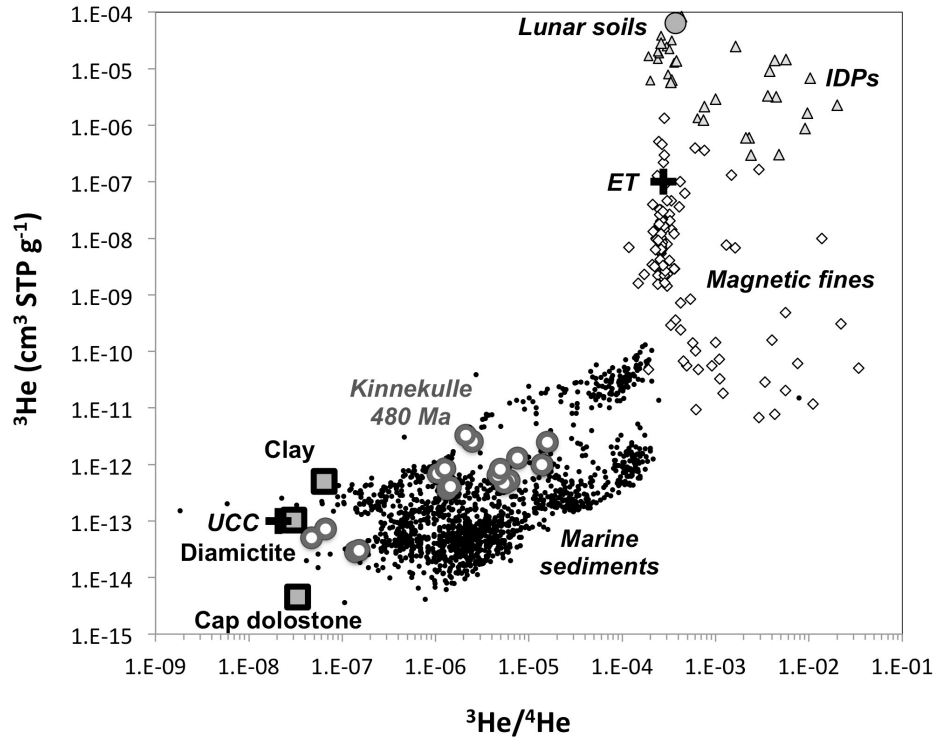

Figure 5 ^{3}He concentrations and ^{3}He/^{4}He for three samples (diamictite, boundary clay, cap carbonate) from the Ravensthroat sections, plotted with marine sediments (small black dots), magnetic particles extracted from marine sediments (open diamonds), IDPs (open triangles; Nier et al., 1990; Nier and Schlutter, 1992), bulk lunar fines (large gray circle, Geiss et al., 1970) and 480 Myr old limestone from Kinnekulle, Sweden (large gray-rimmed circles, Patterson et al., 1998). Mixing lines between bulk lunar fines (ET) and UCC are strongly curved concave up with increasingly positive slope.

4.2. Section 080705.01

The geochemical structure of this section is slightly more complex than that of the Ravensthroat sections. The lithologic boundary at ~100 cm depth is characterized by a ~10-fold spike in Pd concentrations to more than 3 ng/g, somewhat broader and less well pronounced concentration peaks in Pt (increase by a factor of ~3 to almost 0.8 ng/g) and Ir (increase by a

factor of 2-3 to ~15 pg/g), and little change in Os concentrations (Fig. 6, top). Variations in $^{187}Re/^{188}Os$ with depth, particularly in the lower portion of the section that includes the diamictites, are a reflection of the bimodal composition of the diamictite with more clay-rich and more carbonate-rich enclaves (Fig. 6, bottom). $^{187}Re/^{188}Os$ values are low near the Pd and Pt concentration anomalies at 100 cm depth. While there is a slight and rather broad minimum in $^{187}Os/^{188}Os$ (~0.65) at that depth, the fine structure across that boundary reveals an ingrowth-corrected increase from ~0.6 to a value of ~0.85 at 100 cm depth. $^{187}Re/^{188}Os$ and age-corrected $^{187}Os/^{188}Os$ increase up section from ~100 cm depth, with $^{187}Os/^{188}Os$ values reaching ~0.9 (Fig. 6, bottom) and Re concentrations increasing by about an order of magnitude (supplemental data table 1). Horizons enriched in Mo (100 cm, 220 cm) do not correspond to those enriched in Re (10-15 cm), indicating complex enrichments of redox-sensitive elements in this section. The CI-chondrite normalized PGE concentrations have fractionated pattern with low Os and Ir concentrations and an order of magnitude higher Pt, Pd and Re concentrations (Fig. 6, bottom). The enrichment of Os relative to Ir, if present, is much less pronounced than in the Ravensthroat sections.

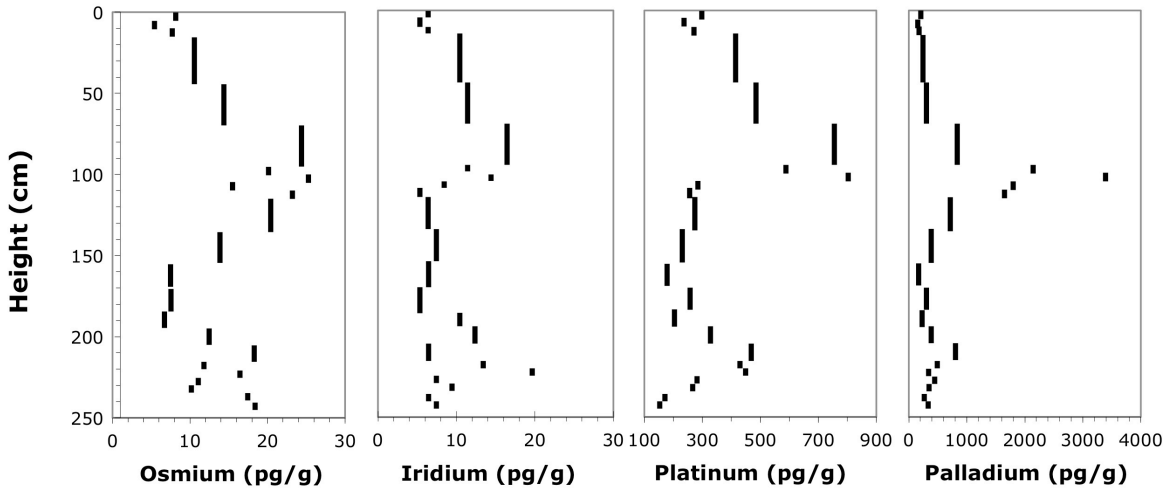

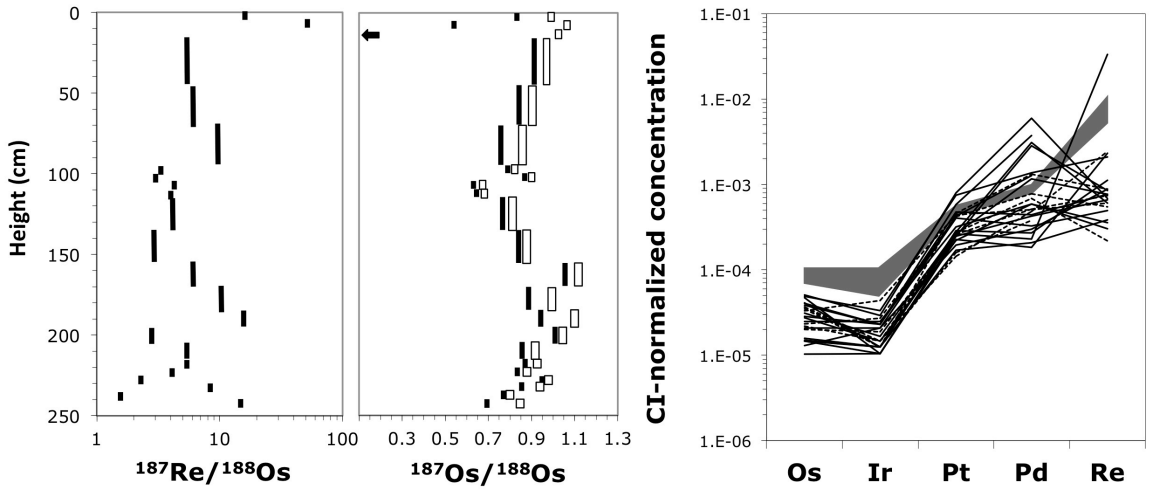

Figure 6 (**top**) Osmium, Ir, Pt, and Pd concentrations in section 080705.01 (P6538, near Fransfontein, NW Namibia). (**bottom**) $^{187}Re/^{188}Os$, $^{187}Os/^{188}Os$ (white: present-day, black: initial; black arrow indicates negative initial ratio), and CI-normalized PGE concentration patterns (solid lines: cap carbonates, stippled lines: diamictites. There is no discernable boundary clay in the same section. Gray field shows UCC composition (Peucker-Ehrenbrink and Jahn, 2001, and references therein).

4.3. Section 081105.04

This section transitions at ~80 cm depth from the underlying Ghaub diamictite into the overlying cap dolostone. The boundary is marked by ~10-fold increases in Pd (up to 2.3 ng/g), Pt (up to 1.6 ng/g), Os (up to 0.8 ng/g) and Ir (up to 0.12 ng/g) concentrations (Fig. 7, top). Rhenium concentrations decrease across the boundary, but increase 10-fold in the 20 cm overlying the lithologic contact (Fig. 7, bottom, and supplemental data table 1). Correspondingly, $^{187}Re/^{188}Os$ value decrease by almost two orders of magnitude at the boundary

370 relative to the diamictites, recovering within ~20 cm of the boundary to values ~30-50 (Fig. 7,
371 bottom). Age-corrected $^{187}Os/^{188}Os$ values increase by ~0.2 units to ~1 at the boundary, decrease
372 to ~0.7 within the overlying 20 cm of cap dolostone and continue to decrease up-section to
373 values of 0.3-0.5.

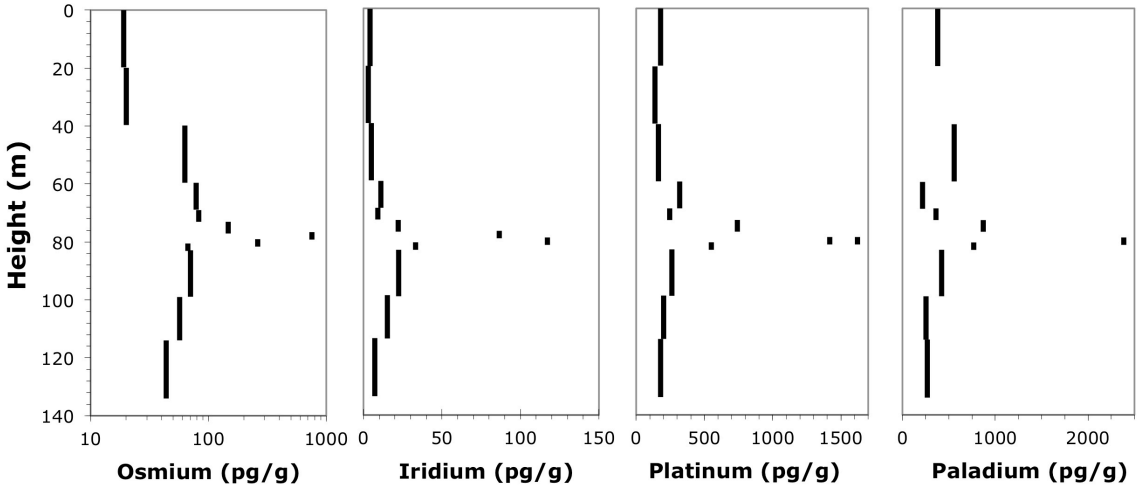

374

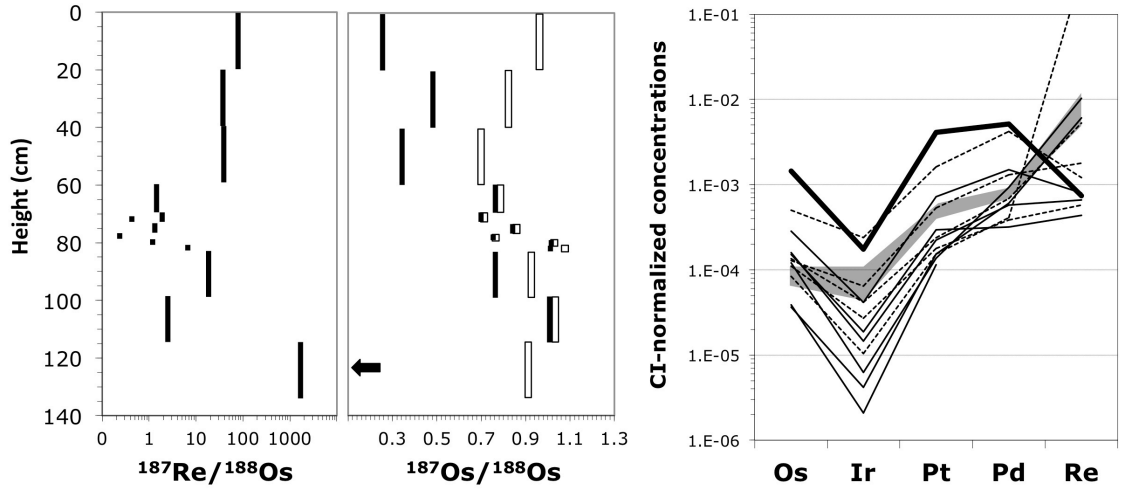

375

376 **Figure 7** **(top)** Osmium, Ir, Pt, and Pd concentrations in section 081105.04 (NW Namibia,
377 19°19.116'S, 013°59.481'E). **(bottom)** $^{187}Re/^{188}Os$, $^{187}Os/^{188}Os$ (white: present-day, black:
378 initial), and CI-normalized PGE concentration patterns in the same section (UCC composition is
379 indicated as gray field, Peucker-Ehrenbrink and Jahn, 2001, and references therein). Black

arrow indicates negative initial ratio. Bold solid black line in CI-normalized PGE concentration pattern indicates boundary clay sample. Thin solid black lines indicate cap carbonate samples, whereas stippled black lines indicate diamictite samples.

CI-normalized PGE concentrations again show a step-like, fractionated abundance pattern with low Ir concentrations and supra-chondritic Os/Ir (Fig. 7, bottom). As in the two other sections, the abundance pattern of the most PGE-rich sample is very similar in shape to those of the other samples and does not become more akin to undifferentiated ET matter (Fig. 7, bottom).

4.4. Replicate Analyses of the Kambishi Core:

As observed in the three sections described above, Ir concentrations in four samples from the original core that Bodiselitsch et al. (2005) investigated do not exceed 0.05 ng/g (K-61=44 pg/g; MJ-6=19 pg/g; MJ-18=35 pg/g; MJ-21=42 pg/g) and are thus far lower than the originally reported values (K-61=1881±85 pg/g; MJ-6=14±7 pg/g; MJ-18=420±40 pg/g; MJ-21=111±21 pg/g; Bodiselitsch et al., 2005). Sample K-61 for which Bodiselitsch et al. (2005) report 1881 pg/g was analyzed twice. The first isotope dilution analyses on 1.01 g sample powder did not yield quantifiable results because the sample was overspiked, indicative of very low Os concentrations in the sample. A replicate, properly spiked isotope dilution analysis on 1.7 g sample material yielded a concentration of 44 pg/g Os. Osmium concentrations in these four previously analyzed samples do not exceed 0.1 ng/g, whereas Pt concentrations reach 1.8 ng/g (MJ-21). Iridium concentrations are even lower, and neither Ir concentrations nor Ir/Al (Fig. 8) yield the anomalies reported by Bodiselitsch et al. (2005). The CI-chondrite normalized PGE abundance pattern shows a step-like pattern with low Os and Ir and elevated Pt concentrations. Measured $^{187}Os/^{188}Os$ are ~ 2, and are not age corrected due to lack of Re data.

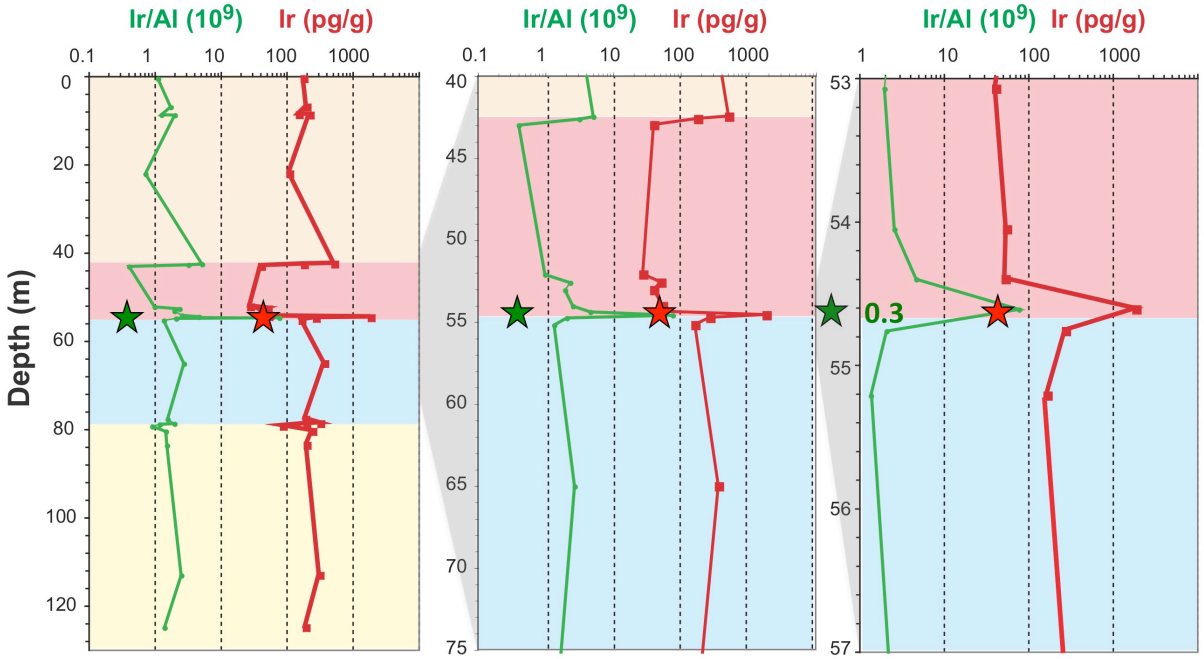

Figure 8 Reanalysis of splits of the Kipushi KH1150PVSSW core (Marinoan section) across the diamictite/cap carbonate transition. Original data from Bodiselitsch et al. (2005) are shown in red (Ir) and green (Ir/Al) lines that connect data points (small squares). Note that Bodiselitsch et al. (2005) did not sample continuously. New data show Ir concentrations (red stars) and Ir/Al data (green stars) for splits of the same samples. Top buff-colored strata: dolomitic shale of the Middle Kundelungu Group, pink: Calcaire Rose, blue: Diamictitie, Petit Conglomerat, bottom buff-colored strata: dolomitic shale of the Upper Nguba Group. Left panel shows the full section (0-130 meters), middle panel shows details between 40 and 75 meters, right panel shows details of the glacial-postglacial transition (53-57 meters).

4.5. Nantuo Tillite and Doushantuo Cap Dolostone, Huajipo Section, Hubei, South China

Four samples taken across the tillite-basal cap dolostone transition show a drop in Os concentrations from ~25 pg/g in the tillite to concentrations of ~2-4 pg/g in the overlying basal Doushantuo cap dolostone (sample C1-2). The boundary clay contains 38 pg/g Os. Measured

(not age corrected) $^{187}Os/^{188}Os$ values decrease from ~0.92 in the tillite to ~0.86 in the boundary clay and in the lowermost portion of the basal cap dolostone (Fig. 2). $^{187}Os/^{188}Os$ values increase to ~0.98 two meters above the contact in the cap limestone (sample C3).

5. Discussion

5.1. PGE Anomalies and their Origin:

This study was intended to investigate whether the reported Ir enrichments at Cryogenian glacial terminations are extraterrestrial in origin and can be used to constrain the duration of ice sheets and sea glaciers during the Marinoan glaciation (Bodiselitsch et al., 2005). Alternatively, the data may provide insights into the accretion rates of ET matter, provided sedimentation rates can be constrained independently with geochronological methods. While we found concentration anomalies of PGE at the transitions from glacial diamictites to overlying cap carbonates, we found little evidence for extraterrestrial contributions to these anomalies. Instead, multiple lines of evidence point to terrestrial sources of PGE enrichments. While we cannot exclude the possibility that differentiated ET material contributed significantly to the observed anomalies, such sources currently constitute a small fraction of ET matter accreted on Earth. Such a source is also contrary to the arguments advanced by Bodiselitsch et al. (2005) who assumed chondritic composition in their calculations of the duration of the glaciations. Most importantly, reanalysis of splits of the core material analyzed by Bodiselitsch et al. (2005) did not yield the reported enrichments in Ir. A potential explanation for this discrepancy could be related to the masses of sediments used for the analyses. Bodiselitsch et al. (2005) used ~0.1 gram of sample material for Instrumental Neutron Activation Analysis (INAA; Bodiselitsch, 2004). The analytical data reported here were done on several grams of material. It is

conceivable that the fortuitous inclusion of small, rare ET particles, possibly only a single particle, in the INAA analyses caused the high Ir and Au concentrations reported by Bodiselitsch et al. (2005). For the sample with the highest concentration reported by Bodiselitsch et al. (2005) a single CI-chondritic particle with 500 ng/g Ir, a density of 3 g/cm^3 and a diameter of ~285 μm can cause the observed Ir concentrations of 1.8 ng/g if only 0.1 g of sediment was analyzed. The chance of having such rare particles affect concentrations is much reduced if significantly larger sample volumes are analyzed. For instance, including a single such particle in the 2-4 g of sediment used in this study only causes Ir concentrations of 0.095 to 0.14 ng/g, similar to values observed by us. This nugget effect is the reason that area-time products of ≥2 m^2 yr^{-1} are needed to obtain reproducible PGE analyses of sediments affected by accumulation of ET matter with a present-day near-Earth particle size distribution (see Peucker-Ehrenbrink and Ravizza, 2000; Peucker-Ehrenbrink, 2001). It is thus possible that the small sample masses used by Bodiselitsch et al. (2005) were not appropriate for the geological application, and that the implications of that study are not statistically significant. The fact that Bodiselitsch et al. (2005) detected concentration anomalies near glacial-postglacial transitions could simply reflect the fact that these transitions were more densely sampled, thereby increasing the likelihood of occasionally encountering rare ET particles in the small sample volumes. The fact that the authors detected concentration anomalies in the diamictites as well as the cap carbonates supports this interpretation. We note that other scenarios for the discrepancies in the analytical results such as contamination during sampling or sample preparation cannot be excluded. It is also possible that anomalous concentrations of ET matter do exist at the transition between glacial and postglacial sediments and that our sampling efforts simply missed those anomalous layers. However, we consider it more likely that the PGE concentration anomalies we observe

461 are equivalent to those found by Bodiselitsch et al. (2005), but are of terrestrial rather than
462 extraterrestrial origin. A lack of evidence for ET signatures in postglacial deposits from NW
463 Namibia was also noted by Gyollai et al. (2014), though the methods used for detecting Ir by
464 INAA were less sensitive than those used by Bodiselitsch et al. (2005), and similar small sample
465 sizes (~0.15 g) were used.

466 *5.2. Sedimentation Rates*

467 The steady flux of ET matter to marine sediments has been used successfully to reconstruct
468 sample-specific sedimentation rates. The three approaches that are based on the most highly
469 enriched elements/isotopes in extraterrestrial vs. terrestrial material are 1) ^{3}He (e.g. Marcantonio
470 et al., 1996, 1998; Higgins et al., 2002; Farley et al., 1997), 2) Os isotopes (e.g. Esser and
471 Turekian, 1993; Pegram and Turekian, 1999; Peucker-Ehrenbrink, 1996), 3) iridium (e.g.
472 Alvarez et al., 1980; Dalai and Ravizza, 2006, 2010), or combinations of them. However, these
473 calculations require preservation of the original geochemical signal that, in the case of the
474 volatile tracer such as He, is not likely. Reconstructions of sedimentation rates that are based on
475 Os isotopes in bulk sediments require an independent reconstruction of the $^{187}Os/^{188}Os$ of
476 contemporaneous seawater, a parameter that is not constrained for the period of the
477 Neoproterozoic investigated here. Partitioning the sedimentary Os isotope budget into an ET
478 component (Meisel et al., 1996; Kurat et al., 1994) and a detrital component with fixed
479 $^{187}Os/^{188}Os$ values for the end-members is likely not appropriate during times of drastically
480 changing environmental conditions in land-proximal environments.

481 We take a different approach that is based on using an element associated with the detrital
482 fraction (Zr, Th, or Ti) to estimate the fraction of bulk Ir ($[Ir]_b$) that is associated with the detrital

483 component for which we assume UCC composition. We further assume that this fraction has an
484 Ir concentration ($[Ir]_{UCC}$) of 22 pg/g and an Os/Ir of ~1 (Peucker-Ehrenbrink and Jahn, 2001).

485 $$[Ir]_{ET} = [Ir]_b - [Ir]_{UCC}\,[Zr]_b/[Zr]_{UCC}$$

486 The choice of crustal indicator element does not change the results significantly. We also
487 assume that the remainder of the Ir is of extraterrestrial origin with an Os/Ir of ~1 (Kurat et al.,
488 1994).

489 $$[Ir]_{ET} = [Os]_{ET}$$

490 The remainder of the Os budget, corrected for radiogenic ingrowth since deposition, is
491 assumed to be of hydrogenous origin, thus explaining observed Os/Ir values >1 in the bulk
492 samples (Figs 4c, 7b). This calculation implies that the samples contain no hydrogenous Ir. As a
493 result, sedimentation rates calculated here are minimum estimates. We further assume ingrowth-
494 corrected (635 Ma) $^{187}Os/^{188}Os$ values of the UCC and ET end-members of 1.0 (Peucker-
495 Ehrenbrink & Jahn, 2001) and 0.12 (Meisel et al., 1996), respectively. This allows us not only to
496 calculate the $^{187}Os/^{188}Os$ of the hydrogenous component, i.e. contemporaneous seawater, but also
497 to estimate the duration of sedimentation (T_{sed}, in kyr) for the depth interval (Δ_{sed}, in cm) each
498 sample encompasses, if we assume that the mass accumulation rate (MAR) of ET osmium to
499 Earth 635 Ma was similar to today (~3 pg Os cm^{-2} kyr^{--1}, Love and Brownlee, 1993; Peucker-
500 Ehrenbrink, 1996).

501 $$IC_{sw} = (IC_b\,[Os]_b - IC_{ET}\,[Os]_{ET} - IC_{UCC}\,[Os]_{UCC}) / ([Os]_b - [Ir]_b)$$

502 $$T_{sed} = \Delta_{sed} / ([Os]_{ET} / MAR_{Os\ ET})$$

503 The results of this 3-component mixing model are shown in Figure 9a-c. We caution that in
504 dynamic land-proximal depositional settings the $^{187}Os/^{188}Os$ as well as Os and Ir concentrations

505 of the detrital component, may vary in time and space much more than in pelagic environments
506 traditionally used to apply tracers of ET matter to constrain sedimentation rates. Despite these
507 caveats, it is instructive to push the interpretation of the geochemical data for the most data-rich
508 sections (Mackenzie Mountains, Canada) to the limit.

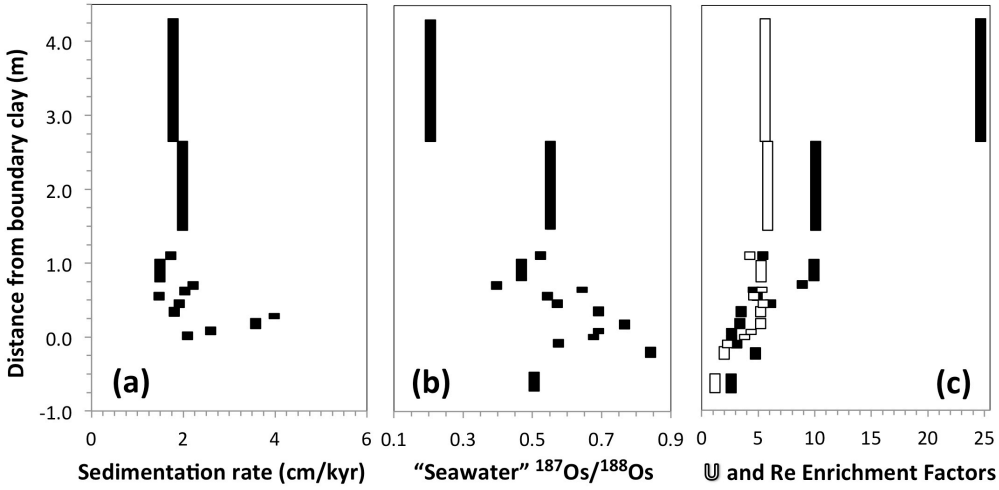

509

510 **Figure 9** (**a**) Estimated sedimentation rates, (**b**) seawater $^{187}Os/^{188}Os$ at time of deposition, and
511 (**c**) uranium (white bars) and rhenium (black bars) enrichment factors relative to average UCC
512 (McLennan, 2001; Peucker-Ehrenbrink and Jahn, 2001). See text for details on the three-
513 component mixing model.

514 We find variable $^{187}Os/^{188}Os$ of postglacial seawater (0.2 to 0.75) for the first 0.25 Myr of cap
515 carbonate deposition (Fig. 9b). Calculated sedimentation rates are between 1.4 and 3.9 cm/kyr
516 with somewhat faster accumulation in the lower 25 cm of the cap carbonates compared to the
517 overlying 4 meters (Fig. 9a). This model assumes present-day accumulation rates of ET matter
518 evenly distributed on Earth (Love and Brownlee, 1993; Peucker-Ehrenbrink, 1996). Faster
519 sedimentation rates would result if some of the non-detrital Ir were seawater-derived
520 (hydrogenous) rather than extraterrestrial in origin. The minimum sedimentation rates estimated

521 from our model are similar to results for slope deposits derived from stable isotope box models
522 (3 cm/kyr) of Kasemann et al. (2014). In contrast, our estimates are much lower than estimates
523 based on sedimentological features and results from climate models (380-1900 cm/kyr). In order
524 to accommodate such fast sedimentation rates, almost all of the non-detrital Ir in the sediments
525 must be hydrogenous rather then extraterrestrial in origin. While we have no tracer for the
526 fraction of Ir that is hydrogenous in origin, using Zr-, Th-, and Ti-normalized Co concentrations
527 to partition bulk Co concentrations into a local detrital (26 μg/g Co vs. 17 μg/g in UCC;
528 McLennan, 2001) and hydrogenous component (Halbach et al., 1983) reveals that 22-57% (Zr-
529 normalized), 0-39% (Th-normalized) or 25-56% (Ti-normalized) of the bulk Co inventories in
530 the cap dolostones are likely of non-detrital origin, suggesting that a significant fraction of the
531 non-detrital Ir is not associated with ET material, but rather hydrogenous in origin. Faster
532 sedimentation rates than the minimum estimates given above are therefore permissible, and our
533 model loses its ability to quantify sedimentation rates as the fraction of hydrogenous Ir in the
534 samples increases.

535 *5.3. Postglacial Environmental Conditions:*

536 The data for all sections reveal systematic trends in the normalized concentrations of redox-
537 sensitive elements, particularly Re and – in the Ravensthroat sections - U, as well as trends in
538 initial $^{187}Os/^{188}Os$ values in the lowermost cap carbonate sections (Fig. 9b). In the Ravensthroat
539 sections, enrichment factors above expected crustal Re concentrations increase from ~2 to ~30
540 from the base to the top of the section (Fig. 9c). In contrast, enrichment factors for U only
541 increase from ~4 to ~10 over the same depth interval. In analogy to modern marine sediments
542 deposited under reducing (sub-oxic to sulfidic) condition, Re is the most strongly enriched
543 redox-sensitive element (Morford and Emerson, 1999). The presence of large marine sinks for

redox-sensitive elements during glaciations, possibly in a synglacial sulfidic ocean (Hurtgen et al., 2006), may have caused a decrease of concentrations of dissolved redox-sensitive metals in glacial seawater. However, low biological productivity under thick ice cover may have left deepwater depleted in organic substrate for microbial sulfate reduction, thereby creating an Fe-rich anoxic but not sulfidic deepwater (cf. Mikucki et al., 2009) with low Re concentrations. Steadily increasing concentrations of redox-sensitive elements in post-glacial seawater may therefore reflect the return to more fully oxygenated seawater. However, it is also possible that the increase in enrichment factors up-section reflects a trend towards more reducing sediments, possibly caused by enhanced deposition, or preservation, of organic matter (Kunzmann et al., 2013), or by upwelling of reducing deepwater (Hurtgen et al., 2006). However, rapid deglaciation would have created a thick, low-density meltwater lid – the "Glacial Lake Harland" of Hoffman (2011) – overlying a cold snowball brine, thereby limiting interaction with the deep ocean. As sedimentary structures and textures in the cap carbonates indicate that the transgressive cap dolostone was deposited in the ocean mixed layer, cap dolostones formed in this meltwater lid and do not represent 'marine' deposits (Shields, 2005; Hoffman, 2011). Whether or how the observed geochemical trends, identified in several sections from different paleogeographic regions, are connected to ocean-wide trends in the evolution of dissolved oxygen, and deposition or preservation of organic carbon (Hurtgen et al., 2006; Sahoo et al., 2012) therefore remains speculative.

The sections dominated by hydrogenous Os (i.e., highest Os/Ir values, Figs 4c, 7b) show decreasing initial $^{187}Os/^{188}Os$ values above the PGE concentration anomalies (Figs. 4b, 7b). Initial $^{187}Os/^{188}Os$ consistently reach ~0.3, indicative of either a more dominant submarine hydrothermal flux or continental inputs dominated by weathering of young mantle-derived rocks.

567 The results from these sections could be interpreted as reflecting the isotopic evolution of local
568 seawater under post-glacial conditions. The fact that the sections that are dominated by
569 hydrogenous Os - including the Ravensthroat sections that allow us to correct for detrital and
570 extraterrestrial contributions - show similar trends could be interpreted as reflected in the
571 inferred global evolution of the low-salinity lid immediately following the Marinoan glaciation.

572 In contrast, the section with Os/Ir values near unity (Fig. 6b) shows no significant temporal
573 change in initial $^{187}Os/^{188}Os$ values above the PGE concentration anomaly (Fig. 6b). Initial
574 $^{187}Os/^{188}Os$ values of 0.7 to 0.9 are somewhat less radiogenic than contemporaneous average
575 UCC inputs ($^{187}Os/^{188}Os$ of ~1.0), assuming that that UCC reservoir has since evolved with an
576 average $^{187}Re/^{188}Os$ of ~35 to present-day values of ~1.4 (Peucker-Ehrenbrink and Jahn, 2001).
577 The slightly less radiogenic composition of the crustal end-member may reflect the nature of the
578 local detrital inputs. However, the local detrital sources do not need to be reflected in the
579 inferred isotope composition of post-glacial seawater, if the residence time of Os in the post-
580 glacial ocean is sufficiently long to reflect a globally integrated weathering signal, similar to the
581 modern marine Os isotope system.

582 ## 6. Conclusion

583 The new data reported here show that PGE concentration anomalies in boundary shales or the
584 lowermost cap carbonates are terrestrial in origin. Replicate analyses of large samples originally
585 analyzed by Bodiselitsch et al. (2005) do not confirm the high Ir concentrations initially reported,
586 but instead show consistently low Ir concentrations, upper crustal PGE concentration pattern and
587 non-chondritic initial $^{187}Os/^{188}Os$. We suspect that undersampling of the ET particle population
588 by using inadequately small sample masses in the original study led to discrepancy between that

589 data and our new data. This conclusion is supported by the helium data, which yielded
590 continental crust isotopic compositions.

591 Concentrations of redox-sensitive elements (Re, U) increase up-section in the lowermost cap
592 carbonates and could be related to increasing marine inventories of these elements after the
593 glaciation, or more poorly oxygenated sediments as the productivity of the post-glacial ocean
594 rebounds. These increases in concentrations are accompanied by variable initial $^{187}Os/^{188}Os$
595 values, each section recording different temporal evolutions from the PGE concentration
596 anomaly to the top of the section. However, geochemical data for the sections that are
597 dominated by hydrogenous Os reveal either an increasingly (up-section) dominant submarine
598 hydrothermal contribution or a continental crust flux that is increasingly dominated by
599 weathering of young mantle-derived lithologies, such as basaltic rocks, following deglaciation.
600 Minimum sedimentation rates for the bottom four meters of cap carbonate deposition in the
601 Mackenzie Mountains (Ravensthroat sections) are estimated to have decreased from a maximum
602 of 4 to a minimum of 2 cm per thousand years from bottom to the top of the sampled section,
603 implying deposition of the bottom ~4 meters of the cap carbonates in less, possibly much less,
604 than 0.24 Myr. These estimates, however, are predicated on the assumption that ET matter
605 deposited during the formation of the sediments investigated here had been accumulating
606 spatially and temporally evenly on the seafloor.

607 ## Acknowledgements

608 We are grateful for support from a 2008 WHOI Summer Student Fellowship for CAW. BPE
609 acknowledges financial support from WHOI's Ocean and Climate Change Institute (CH11320)
610 and U.S. NSF SGER grant EAR-0821878. Fieldwork in NW Canada was licensed by the Aurora

611 Research Institute and supported by a grant to PFH from the Astrobiology Institute of the US
612 National Aeronautics and Space Administration (NASA). Fieldwork in NW Canada and
613 Namibia was supported by grants EAR-9905495 and EAR-0417422 (to PFH) from the US NSF.
614 We thank Jon Husson (Harvard University) and Ricardo Trindade (University of São Paulo,
615 Brazil) for excellent support during fieldwork in Namibia in August of 2005. Adam Maloof and
616 Cin-Ty Lee kindly shared samples used in this study, and Sharad Master (University of
617 Witwatersrand, South Africa) kindly provided splits of some of the original sediments analyzed
618 by Bodiselitsch et al. (2005). We thank Tracy Atwood and Joshua Curtice for assistance with the
619 PGE-Re-Os analyses in the WHOI ICPMS facility and He isotope analyses in the WHOI IGF,
620 respectively. Christian Koeberl graciously sent us a copy of Bernd Bodiselitsch's dissertation.
621 Careful reviews by Alan Rooney and an anonymous reviewer greatly helped to refine the
622 presentation of our findings.

623 ## References

624 Abbot, D.S., Pierrehumbert, R.T., 2010. Mudball: Surface dust and Snowball Earth deglaciation.
625 J. Geophys. Res., doi: 10.1029/2009JD012007.
626 Abbot, D.S., Voigt, A., Koll, D. 2011. The Jormungand global climate state and implications for
627 Neoproterozoic glaciations. J. Geophys. Res. 116, D18103, doi: 10.1029/2011JD015927.
628 Abbot, D.S., Voigt, A., Li Dawei, Le Hir, G., Pierrehumbert, R.T., Branson, M., Pollard, D.,
629 Koll, D.D.B., 2013. Robust elements of Snowball Earth atmospheric circulation and oases for
630 life. J. Geophys. Res.: Atmospheres 118, 6017-6027, doi:10.1002/jgrd.50540.
631 Alvarez, L.W., Alvarez, W., Asaro, F., Michel, H.V., 1980. Extraterrestrial cause for the
632 Cretaceous-Tertiary extinction. Science 208, 1095-1108.

633 Bao, H., Lyons, J.R., Zhou, C. 2008. Triple oxygen isotope evidence for elevated CO_2 levels
634 after a Neoproterozoic glaciation. Nature 452, 504-506.
635 Bodiselitsch, B., 2004. Geochemical and stable isotope investigations on "Snowball Earth"
636 samples from the Lufilian tectonic arc, D. R. Congo and Zambia, and on late Eocene
637 sediment samples from Massignano, Italy. Doctoral Dissertation, Universität Wien, 124 p.
638 Bodiselitsch, B., Koeberl, C., Master, S., Reimold, W.U., 2005. Estimating duration and intensity
639 of Neoproterozoic snowball glaciations from Ir anomalies. Science 308, 239-242.
640 Calver, C.R., Crowley, J.L., Wingate, M.T.D., Evans, D.A.D., Raub, T.D., Schmitz, M.D. 2013.
641 Globally synchronous Marinoan deglaciation indicated by U-Pb geochronology of the
642 Cottons Breccia, Tasmania, Australia. Geology 41, 1127-1130.
643 Condon, D., Zhu, M., Bowring, S., Wang, W., Yang, A., Jin, Y., 2005. U-Pb ages from the
644 Neoproterozoic Doushantuo Formation, China. Science 308, 95-98.
645 Dalai, T., Ravizza, G., 2006. Evaluation of osmium isotope and iridium as paleoflux tracers in
646 pelagic carbonates. Geochim. Cosmochim. Acta 70, 3928-3942.
647 Dalai, T., Ravizza, G., 2010. Investigation of an early Pleistocene marine osmium isotope record
648 from the eastern equatorial Pacific. Geochim. Cosmochim. Acta 74 (15), 4332-4345.
649 Embleton, B.J.J., Williams, G.E., 1986. Low latitude of deposition for late Precambrian
650 periglacial varvites in South Australia: implications for palaeoclimatology. Earth Planet. Sci.
651 Lett. 79, 419-430.
652 Esser, B.K., Turekian, K.K., 1993. The osmium isotopic composition of the continental crust.
653 Geochim. Comochim. Acta 57, 3093-3014.
654 Evans, D.A.D., 2000. Stratigraphic, geochronological, and paleomagnetic constraints upon the
655 Neoproterozoic climatic paradox. Am. J. Sci. 300, 347-433.

656 Evans, D.A.D., 2003. A fundamental Precambrian–Phanerozoic shift in earth's glacial style?
657 Tectonophysics 375, 353-385.
658 Evans, D.A.D., 2006. Proterozoic low orbital obliquity and axial-dipolar geomagnetic field from
659 evaporite palaeolatitudes. Nature 444, 51-55.
660 Evans, D.A.D., Raub, T.D., 2011. Neoproterozoic glacial palaeolatitudes: a global update. In:
661 Arnaud, E., Halverson, G.P., Shields-Zhou, G. (Eds.) The Geological Record of
662 Neoproterozoic Glaciations. Geological Society, London, Memoir 36, pp. 93-112.
663 Farley, K.A., Love, S.G., Patterson, D.B., 1997. Atmospheric entry heating and helium
664 retentivity of interplanetary dust particles. Geochim. Cosmochim. Acta 61, 2309-2316.
665 Ferreira, D., Marshall, J., O'Gorman, P. A., Seager, S., 2014. Climate at high-obliquity. Icarus
666 243, 236-248.
667 Font, E., Nedelec, A., Trindade, R.I.F., Moreau, C., 2010. Fast or slow melting of the Marinoan
668 snowball Earth? The cap dolostone record. Palaeogeogr., Palaeoclim., Palaeoecol. 295, 215-
669 225.
670 Geiss, J., Eberhardt, P., Bühler, F., Meister, J., Signer, P., 1970. Apollo 11 and 12 solar wind
671 composition experiments: Fluxes of He and Ne isotopes. J. Geophys. Res., Space Phys. 75,
672 5972-5979.
673 Goderis, S., Tagle, R., Belza, J., Smit, J., Montanari, A., Vanhaecke, F., Erzinger, J., Claeys, Ph.,
674 2013. Reevaluation of siderophile element abundances and ratios across the Cretaceous-
675 Paleogene (K-Pg) boundary: Implications for the nature of the projectile. Geochim.
676 Cosmochim. Acta 120, 417-446.
677 Goodman, J., Pierrehumbert, R.T., 2003. Glacial flow of floating marine ice in "Snowball
678 Earth". J. Geophys. Res. 108 (C10), 3308, doi:10.1029/2002JC001471.

679 Gordey, S.P., MacDonald, J., Roots, C.F., Fallas, K.M., Martel, E., 2010. Regional cross-
680 sections, detachment levels and origin of the Plateau Fault, central Mackenzie Mountains,
681 Northwest Territories. Geol. Surv. Canada, Open File 6593, scale 1:100,000.
682 Gradstein, J.F., Ogg, J.G., Schmitz, M.D., Ogg, G.M., 2012. The Geologic Time Scale 2012,
683 Vol. 1, Elsevier, Amsterdam, 435 pages.
684 Gyollai, I., Mader, D., Polgàri, M., Popp, F., Koeberl, C., 2014. Lack of evidence for impact
685 signatures in Neoproterozoic postglacial deposits from NW-Namibia. Austrian J. Earth Sci.
686 107, 100-111.
687 Halbach, P., Segl, M., Puteanus, D., Mangini, A., 1983. Co-fluxes and growth rates in
688 ferromanganese deposits from central Pacific seamount areas. Nature 304, 716-719.
689 Harland, W.B., 1964. Evidence of late Precambrian glaciation and its significance. *In:* Nairn,
690 A.E.M. (Ed.) Problems in Palaeoclimatology. Interscience, London, p. 119-149.
691 Hassler, D.R., Peucker-Ehrenbrink, B., Ravizza,G.E., 2000. Rapid determination of Os isotopic
692 compositions by sparging OsO_4 into a magnetic-sector ICP-MS. Chem. Geol. 166, 1-14.
693 Higgins, S.M., Anderson, R.F., Marcantonio, F., Schlosser, P., Stute, M., 2002. Sediment
694 focusing creates 100-ka cycles in interplanetary dust accumulation on the Ontong Java
695 Plateau. Earth Planet. Sci. Lett. 203, 383-397.
696 Hodson, M.E., 2002. Experimental evidence for mobility of Zr and other trace elements in soils.
697 Geochim. Cosmochim. Acta 66, 819-828.
698 Hoffman, P.F., Kaufman, A.J., Halverson, G.P., Schrag, D.P., 1998. A Neoproterozoic snowball
699 Earth. Science 281, 1342-1346.
700 Hoffman, P.F., Schrag, D.P., 2002. The snowball Earth hypothesis: testing the limits of global
701 change. Terra Nova 14, 129-155.

Hoffman, P.F., 2005. 28th DeBeers Alex. Du Toit Memorial Lecture, 2004, On Cryogenian (Neoproterozoic) ice-sheet dynamics and the limitations of the glacial sedimentary record. South African J. Geol. 108, 557-576.

Hoffman, P.F., Halverson, G.P., Domack, E.W., Husson, J.M., Higgins, J.A., Schrag, D.P., 2007. Are basal Ediacaran (635 Ma) post-glacial "cap dolostones" diachronous? Earth Planet. Sci. Lett. 258, 114-131.

Hoffman, P.F., Halverson, G.P., 2008. Otavi Group of the western Northern Platform, the Eastern Kaoko Zone and the western Northern Margin Zone. In: Miller, R. McG. (Ed.) The Geology of Namibia, vol. 2. Handbook of the Geological Survey of Namibia, Windhoek, pp. 13.69-13.136.

Hoffman, P.F., 2011. Strange bedfellows: glacial diamictite and cap carbonate from the Marinoan (635 Ma) glaciation in Namibia. Sedimentology 58, 57-119.

Hoffman, P.F., Macdonald, F.A., Halverson, G.P., 2011. Chemical sediments associated with Neoproterozoic glaciation: iron formation, cap carbonate, barite and phosphorite. In: Arnaud, E., Halverson G.P., Shields-Zhou, G. (eds) The Geological Record of Neoproterozoic Glaciations. Geological Society, London, Memoir 36, pp. 67-80.

Hoffmann, K.-H., Condon, D.J., Bowring, S.A., Crowley, J.L., 2004. U-Pb zircon date from the Neoproterozoic Ghaub Formation, Namibia: constraints on Marinoan glaciation. Geology 32, 817-820, doi:10.1130/G20519.l

Hurtgen, M.T., Halverson, G.P., Arthur, M.A., Hoffman, P.F., 2006. Sulfur cycling in the aftermath of a 635-Ma snowball glaciation: Evidence for a syn-glacial sulfidic deep ocean. Earth Planet. Sci. Lett. 245, 551-570.

724 James, N.P., Narbonne, G.M., Kyser, T.K. 2001. Late Neoproterozoic cap carbonates:
725 Mackenzie Mountains, northwestern Canada: precipitation and global glacial meltdown.
726 Can. J. Earth Sci. 38, 1229-1262.
727 Kasemann, S.A., Pogge von Strandmann, P.A.E., Prave, A.R., Fallick, A.E., Elliot, T.,
728 Hoffmann, K.-H., 2014. Continental weathering following a Cyrogenian glaciation: Evidence
729 from calcium and magnesium isotopes. Earth Planet. Sci. Lett. 396, 66-77.
730 Kennedy, M.J. 1996. Stratigraphy, sedimentology, and isotopic geochemistry of Australian
731 Neoproterozoic postglacial cap dolostones: deglaciation, $d^{13}C$ excursions, and carbonate
732 precipitation. J. Sed. Res. 66, 1050-1064.
733 Kennedy, M.J., Runnegar, B., Prave, A.R., Hoffmann, K.-H., Arthur, M.A. 1998. Two or four
734 Neoproterozoic glaciations? Geology 26, 1059-1063.
735 Kirschvink, J.L., 1992. Late Proterozoic low-latitude glaciation: the snowball Earth. In: The
736 Proterozoic Biosphere (Schopf, J.W., C Klein, C., Eds.), Cambridge Univ. Press, Cambridge,
737 pp. 51-52.
738 Knoll, A.H., Walter, M.R., Narbonne, G.M., Christie-Blick, N. 2006. The Ediacaran Period: a
739 new addition to the geologic time scale. Lethaia 39, 13-30.
740 Kunzmann, M., Halverson, G.P., Sossi, P.A., Raub, T.D., Payne, J.L., Kirby, J., 2013. Zn isotope
741 evidence for immediate resumption of primary productivity after snowball Earth. Geology
742 41, 27-30.
743 Kurat, G., Koeberl, C., Presper, T., Brandstätter, F., Maurette, M., 1994. Petrology and
744 geochemistry of Antarctic micrometeorites. Geochim. Cosmochim. Acta 58, 3879-3904.

745 Kurz, M.D., Curtice, J., Lott III, D.E., Solow, A., 2004. Rapid helium isotopic variability in
746 Mauna Kea shield lavas from the Hawaiian Scientific Drilling Project. Geochem. Geophys.
747 Geosyst. 5 (4), Q04G14, doi: 10.1029/2002GC000439.
748 Laskar, J., Joutel, F., Roboutel, P., 1993. Stabilization of the Earth's obliquity by the Moon.
749 Nature 361, 615-617.
750 Li, D., Pierrehumbert, R.T., 2011. Sea glacier flow and dust transport on Snowball Earth.
751 Geophys. Res. Lett. 38, L17501, doi:10.1029/2011GL048991
752 Li, Z.X., Evans, D.A.D., Halverson, G.P. 2013. Neoproterozoic glaciations in a revised global
753 palaeogeography from the breakup of Rodinia to the assembly of Gondwanaland. Sed.
754 Geol. 294, 219-232.
755 Love, S.G., Brownlee, D.E., 1993. A direct measurement of the terrestrial mass accretion rate of
756 cosmic dust. Science 262, 550-553.
757 Macdonald, F.A., Schmitz, M.D., Crowley, J.L., Roots, C.F., Jones, D.S., Maloof, A.C., Strauss,
758 J.V., Cohen, P.A., Johnston, D.T., Schrag, D.P., 2010. Calibrating the Cryogenian. Science
759 327, 1241-1243.
760 Macdonald, F.A., Strauss, J.V., Speling, E.A., Halverson, G.P., Narbonne, G.M., Johnston, D.T.,
761 Kunzmann, M., Schrag, D.P., Higgins, J.A., 2013. The stratigraphic relationship between the
762 Shuram carbon isotope excursion, the oxygenation of Neoproterozoic oceans, and the first
763 appearance of the Ediacara biota and bilaterian trace fossils in northwest Canada. Chem.
764 Geol. 362, 250-272.
765 MacNaughton, R.B., Fallas, K.M., W Zantvoort, W., 2008. Qualitative assessment of the Plateau
766 Fault (Mackenzie Mountains, NWT) as a conceptual hydrocarbon play. Geol. Surv. Canada,
767 Open File 5831, 29 p.

768 Marcantonio, F., Anderson, R.F., Stute, M., Kumar, N., Schlosser, P., Mix, A., 1996.
769 Extraterrestrial ^{3}He as a tracer of marine sediment accumulation. Nature 383, 705-707.
770 Marcantonio, F., Higgins, S., Anderson, R.F., Stute, M., Schlosser, P., Rusbury, E.T., 1998.
771 Terrigenous helium in deep-sea sediments. Geochim. Cosmochim. Acta 62, 1535-1543.
772 Marcantonio, F., Turekian, K.K., Higgins, S., Anderson, R.F., Stute, M., Schlosser, P., 1999. The
773 accretion rate of extraterrestrial ^{3}He based on oceanic ^{230}Th flux and the relation to Os
774 isotope variation over the past 200,000 years in an Indian Ocean core. Earth Planet. Sci. Lett.
775 170, 157-168.
776 McLennan, S.M., 2001. Relationship between the trace element composition of sedimentary
777 rocks and upper continental crust. Geochem. Geophys. Geosyst. 2 (4), doi:
778 10.1029/2000GC000109.
779 Meisel, T., Walker, R.J., Morgan, J.W., 1996. The osmium isotopic composition of the Earth's
780 primitive upper mantle. Nature 383, 517-520.
781 Mikucki, J.A., Pearson, A., Johnston, D.T., Turchyn, A.V., Farquhar, J., Schrag, D.P., Anbar,
782 A.D., Priscu, J.C., Lee, P.A., 2009. A contemporary microbially maintained subglacial
783 ferrous "ocean". Science 324, 397-400.
784 Miller, C.A., Peucker-Ehrenbrink, B., Walker, B.D., Marcantonio, F., 2011. Re-assessing the
785 surface cycling of molybdenum and rhenium. Geochim. Cosmochim. Acta 75, 7146-7179.
786 Morford, J.L., Emerson, S., 1999. The geochemistry of redox sensitive trace elements in
787 sediments. Geochim. Cosmochim. Acta 63, 1735-1750.
788 Nier, A.O., Schlutter, D.J., Brownlee, D.E., 1990. Helium and neon isotopes in deep Pacific
789 Ocean sediments. Geochim. Cosmochim. Acta 54, 173-182.

790 Nier, A.O., Schlutter, D.J., 1992. Extraction of helium from individual interplanetary dust
791 particles by step-heating. Meteoritics 27, 166-173.
792 Patterson, D.B., Farley, K.A., Schmitz, B., 1998. Preservation of extraterrestrial ^{3}He in 480-Ma-
793 old marine limestones. Earth Planet. Sci. Lett. 163, 315-325.
794 Pegram, W.J., Turekian, K.K., 1999. The osmium isotopic composition change of Cenozoic sea
795 water as inferred from a deep-sea core corrected for meteoritic contributions. Geochim.
796 Cosmochim. Acta 63, 4053-4058.
797 Peucker-Ehrenbrink, B., 1996. Accretion of extraterrestrial matter during the last 80 million
798 years and its effect on the marine Os isotope record. Geochim. Cosmochim. Acta 60, 3187-
799 3196.
800 Peucker-Ehrenbrink, B., Ravizza, G.E., 2000. The effects of sampling artifacts on cosmic dust
801 flux estimates: A reevaluation of nonvolatile tracers (Os, Ir). Geochim. Cosmochim. Acta 64,
802 1965-1970.
803 Peucker-Ehrenbrink, B., 2001. Iridium and osmium as tracers of extraterrestrial matter in marine
804 sediments. In: Peucker-Ehrenbrink, B., Schmitz, B., (Eds.) Accretion of Extraterrestrial
805 Matter Throughout Earth's History, Kluwer Acad./Plenum Publ., New York, 163-178.
806 Peucker-Ehrenbrink, B., Jahn, B.-m., 2001. Rhenium-osmium isotope systematics and platinum
807 group element concentrations: Loess and the upper continental crust. Geochem. Geophys.
808 Geosyst. 2 (10), 2200, doi:10.1029/2001GC000172.
809 Peucker-Ehrenbrink, B., Bach, W., Hart, S.R., Blusztajn, J.S., Abbruzzese, T., 2003. Rhenium-
810 osmium isotope systematics and platinum group element concentrations in oceanic crust
811 from DSDP/ODP Sites 504 and 417/418. Geochem. Geophys. Geosyst. 4 (7), 8911, doi:
812 10.1029/2002GC000414.

813 Peucker-Ehrenbrink, B., Hanghoj, K., Atwood, T., Kelemen, P.B., 2012. Rhenium-osmium
814 isotope systematics and platinum group element concentrations in oceanic crust. Geology,
815 G32733, doi: 10.1130/G32431.1.
816 Pierrehumbert, R.T., Abbot, D.S., Voigt, A., Koll, D., 2011. Climate of the Neoproterozoic.
817 Annual Reviews Earth Planet. Sci. 39, 417-460.
818 Ravizza, G.E., Pyle, D., 1997. PGE and Os isotope analyses of single sample aliquots with NiS
819 fire assay preconcentration. Chem. Geol. 141, 251-268.
820 Rodehacke, C.B., Voigt, A., Ziemen, F., Abbot, D.S., 2013. An open ocean region in
821 Neoproterozoic glaciations would have to be narrow to allow equatorial ice sheets. Geophys.
822 Res. Lett. 40 (20), 5503-5507.
823 Rooney, A.D., Strauss, J.V., Brandon, A.D., Macdonald, F.A. 2015. A Cryogenian chronology:
824 Two long-lasting synchronous Neoproterozoic glaciations. Geology 43, 459-462.
825 Rose, B.E.J., 2015. Stable "Waterbelt" climates controlled by tropical ocean heat transport: A
826 nonlinear coupled climate mechanism of relevance to Snowball Earth. J. Geophys. Res. 120,
827 doi: 10.1002/2014JD022659.
828 Sahoo, S.K., Planavsky, N.J., Kendall, B., Wang, X., Shi, X., Scott, C., Anbar, A.D., Lyons,
829 T.W., Jiang, G., 2012. Ocean oxygenation in the wake of the Marinoan glaciation. Nature
830 489, 546-549, doi: 10.1038/nature11445.
831 Schmidt, P.W., Williams, G.E., Embleton, B.J.J., 1991. Low palaeolatitude of Late Proterozoic
832 glaciation: early timing of remanence in haematite of the Elatina Formation, South Australia.
833 Earth Planet. Sci. Lett. 105, 355-367.
834 Schmitz, B., Peucker-Ehrenbrink, B., Lindström, M., Tassinari, M., 1997. Accretion rates of
835 meteorites and extraterrestrial dust in the Early Ordovician. Science 278, 88-90.

836 Schulte, P., Alegret, L., Arenillas, I., and 38 additional co-authors, 2010. The Chicxulub asteroid
837 impact and mass extinction at the Cretaceous-Paleogene Boundary. Science 327, 1214-1218,
838 doi: 10.1126/science.1177265.
839 Sen, I.S., Peucker-Ehrenbrink, B., 2014. Determination of osmium concentrations and
840 $^{187}Os/^{188}Os$ of crude oils and source rocks by coupling high-pressure, high-temperature
841 digestion with sparging OsO_4 into a multicollector inductively coupled plasma mass
842 spectrometer. Anal. Chem. 86, 2982-2988, doi: 10.1021/ac403413y.
843 Shields, G.A., 2005. Neoproterozoic cap carbonates: a critical appraisal of existing models and
844 the plumeworld hypothesis. Terra Nova 17, 299-310.
845 Sohl, L.E., Christie-Blick, N., Kent, D.V., 1999. Paleomagnetic polarity reversals in Marinoan
846 (ca 600 Ma) glacial deposits of Australia: implications for the duration of low-latitude
847 glaciation in Neoproterozoic time. Geol. Soc. Amer. Bull. 111, 1120-1139.
848 Tredoux, M., de Wit, M.J., Hart, R.J., Lindsay, N.M., Verhagen, B., Sellschop, J.P.F., 1989.
849 Chemostratigraphy across the Cretaceous-Tertiary boundary and a critical assessment of the
850 iridium anomaly. J. Geol. 97, 585-605.
851 Voigt, A., Abbot, D.S., 2012. Sea-ice dynamics strongly promote Snowball Earth initiation and
852 destabilize tropical sea-ice margins. Climate of the Past 8, 2445-2475.
853 Warren, S.G., Brandt, R.E., Grenfell, T.C., McKay, C.P., 2002. Snowball Earth: Ice thickness on
854 the tropical ocean. J. Geophys. Res. 107 (C10), 3167, doi:10.1029/2001JC001123.
855 Williams, G.E., 1975. Late Precambrian glacial climate and the Earth's obliquity. Geol. Mag.
856 112, 441-544.

857 **Supplemental Data Table (Table S1)**

SARM ID	SE 1	SE 2	SE 3				SE 4	SE 5	SE 6	SE 7	SE 8	SE 9	SE 10			SE 11	SE 12	SE 13	SE 14	SE 15	SE 16		SE 17	SE 18
WHOI ID	1850	1851	1852	1832	1722		1853	1854	1855	1856	1857	1858	1859	1833	1721	1860	1861	1862	1889	1890	1891B	1919	1893	1892
Section	GR	GR	GR	GR	GR	GR	GR	GR	GR	GR	GR	GR	GR	GR	GR	GR	GR	GR	CR	CR	SKR	SKR	SKR	SKR
Mass. Spec.	E2	E2	E2	E2	N/E2	N/E2	E2	E2	E2	E2	E2	E2	E2	E2	N	E2	E2	E2	N	N	N	N	N	N
Sample Name	P1 0.0	P1 0.05	P1 0.1	P1 0.25		P1 0.25 filters	P1 0.28	P1 0.4	P1 0.5	P1 0.6	P1 0.65	P1 0.75	P1 1.05	P1 1.15		P1 1.45	P1 2.65	P1 4.3	P4A-346-7	P4A-364-9	P5B-0.05	duplicate	P5B-0.30	P5B-15
Sample wt (g)																								
187Os/188Os	0.6992	0.685	0.724	0.7172	0.670	0.694	0.730	0.729	0.741	0.728	0.7508	0.7772	0.755	0.7578	0.727	0.792	0.8211	1.028	0.5984	0.5003	0.5645	0.5748	0.5894	0.7987
±2 s.d.	0.0013	0.006	0.016	0.0034	0.007	0.007	0.009	0.009	0.007	0.007	0.0027	0.0033	0.005	0.0034	0.006	0.004	0.0018	0.007	0.0017	0.0011	0.0012	0.0032	0.0015	0.0025
(all pg/g)																								
Os	33	28	30	23	24	250	18	15	14	16	14	17	11	18	18	18	23	20	174	241	1261	1304	153	456
% blank corr.	3	3	3	4	4		5	5	6	5	6	5	7	5	5	5	4	4	0.5	0.4	0.1	0.1	0.6	0.2
Ir	3.9	4.2	5.3	4.7	2.7	4.5	3.2	3.3	3.0	3.5	3.8	2.8	3.1	3.5	1.6	3.3	3.1	3.0	49	78	83	74	61	122
Bodiselitsch Ir																								
Pd	255	239	247	218	316	438	233	175	177	229	182	235	273	276	251	182	250	186	2948	2327	3062	2665	2284	3420
% s.d.	2	3	3	2	26	16	3	4	4	4	5	3	3	2	35	5	3	7	4	5	4	1	5	4
Pt	284	160	165	210	203	200	139	111	138	120	126	116	132	96	207	88	147	131	1633	1263	4468	4764	1443	2646
% s.d.	0	0	0	0	8	4	1	1	1	1	1	1	1	1	9	1	0	1	1	1	0	0	1	0
Re	30	25	29				31	55	54	43	92	99	51			89	241	241	375	197	392		2431.51	920
187Re/188Os	4.75	4.61	5.08				9.03	18.89	20.06	13.50	34.04	29.83	24.76			26.12	55.99	66.38	11.02	4.14	1.58		81.25	10.59
187Os/188Os (635 Ma initial)	0.649	0.636	0.670				0.634	0.528	0.528	0.585	0.389	0.460	0.492			0.514	0.226	0.322	0.481	0.456	0.548		-0.275	0.686
Sample wt (g)		8.2365																			0.9188		1.5683	
3He pcc/g		0.004569																			0.5012		0.1039	
4He µcc/g		0.1360																			7.7820		3.3730	
3He/4He (R/Ra)		0.024																			0.046		0.022	
(all µg/g)																								
As	bdl	bdl	bdl				bdl	bdl	bdl	bdl	bdl	bdl	bdl			bdl	bdl	2.47	3.4	15.1	6.0		4.3	8.8
Ba	42	33	33		e		30	30	48	56	35	31	35			21	58	32	282	391	303		519	420
Be	bdl	bdl	bdl				bdl	bdl	bdl	bdl	bdl	bdl	bdl			bdl	bdl	bdl	2.0	2.6	1.5		2.2	3.6
Bi	bdl	bdl	bdl				bdl	bdl	bdl	bdl	bdl	0.12	bdl			bdl	bdl	bdl	0.23	0.66	0.19		0.33	0.50
Cd	0.43	0.45	0.55				0.49	0.48	0.39	0.41	0.39	0.50	bdl			bdl	0.36	bdl	bdl	0.33	0.27		bdl	bdl
Ce	6.5	4.7	4.6				4.7	4.7	5.2	5.0	5.2	4.9	4.8			4.7	5.1	4.3	50.8	63.0	71.5		65.5	89.7
Co	1.9	1.5	1.6				1.6	1.7	1.8	1.5	1.9	1.8	1.6			1.4	2.2	1.5	12.8	53.1	20.6		25.3	34.7
Cr	bdl	bdl	bdl				4.2	4.2	5.3	4.7	4.9	4.6	4.8			4.6	4.2	bdl	60.8	92.9	51.4		84.3	118
Cs	bdl	bdl	bdl				bdl	bdl	bdl	bdl	bdl	bdl	bdl			bdl	bdl	bdl	4.4	6.4	4.0		7.4	11.2
Cu	4.4	4.8	5.4				4.8	4.4	5.4	3.9	7.6	6.7	4.5			bdl	7.0	3.8	145	107	13.7		23.9	36.3
Dy	0.71	0.44	0.43				0.35	0.35	0.39	0.41	0.39	0.39	0.32			0.32	0.38	0.30	3.81	4.85	6.84		5.05	6.21
Er	0.42	0.26	0.26				0.21	0.20	0.23	0.23	0.23	0.22	0.18			0.17	0.20	0.17	2.19	3.09	3.71		2.79	3.45
Eu	0.19	0.13	0.13				0.12	0.11	0.13	0.13	0.13	0.12	0.10			0.09	0.11	0.09	0.94	1.05	1.68		1.297	1.59
Ga	1.44	0.97	1.03				0.90	0.89	1.37	1.54	0.94	0.98	0.96			0.57	1.37	0.99	14.8	22.9	12.4		19.7	27.5
Gd	0.84	0.52	0.51				0.43	0.44	0.48	0.51	0.49	0.48	0.40			0.39	0.44	0.36	3.93	4.68	7.93		5.71	6.97
Ge	0.08	0.08	0.07				0.09	0.08	0.08	0.10	0.07	0.07	0.07			0.08	0.16	0.13	1.82	2.10	1.21		2.16	2.53
Hf	0.30	0.27	0.23				0.22	0.22	0.25	0.22	0.23	0.21	0.23			0.20	0.22	0.19	4.12	5.50	3.39		5.89	5.36
Ho	0.14	0.09	0.09				0.07	0.07	0.08	0.08	0.08	0.08	0.07			0.06	0.07	0.06	0.75	1.02	1.34		0.98	1.20
In	bdl	bdl	bdl				bdl	bdl	bdl	bdl	bdl	bdl	bdl			bdl	bdl	bdl	0.08	0.10	0.10		0.06	0.08
La	3.12	2.27	2.25				2.32	2.32	2.45	2.35	2.47	2.23	2.20			2.11	2.38	2.14	24.5	31.0	29.4		32.6	44.1
Lu	0.08	0.04	0.04				0.03	0.03	0.04	0.04	0.04	0.04	0.03			0.03	0.03	0.03	0.35	0.54	0.56		0.45	0.54
Mo	bdl	bdl	bdl				bdl	bdl	bdl	bdl	bdl	bdl	bdl			bdl	bdl	bdl	bdl	0.74	bdl		bdl	0.96
Mo (ng/g) ID																								
Nb	1.26	0.88	0.80				0.62	0.60	0.69	0.58	0.60	0.61	0.62			0.57	0.64	0.53	8.58	14.5	9.18		10.5	13.9
Nd	3.64	2.37	2.35				2.17	2.18	2.49	2.59	2.54	2.53	2.29			2.12	2.54	2.02	23.3	27.9	35.9		29.0	40.5
Ni	9.73	7.84	8.23				10.72	10.11	11.02	10.39	11.09	9.80	7.34			7.11	8.70	6.51	30.3	98.0	76.9		59.6	102
Pb	0.97	3.38	1.82				1.20	1.11	bdl	0.91	1.03	1.25	1.14			1.30	1.14	0.97	10.9	45.4	8.56		17.6	25.3
Pr	0.87	0.59	0.59				0.57	0.56	0.65	0.66	0.66	0.63	0.60			0.57	0.65	0.54	6.12	7.43	8.61		7.79	10.6
Rb	7.09	5.35	5.47				4.81	4.68	7.27	8.25	5.23	4.92	5.08			2.98	7.06	5.40	105	150	79.1		152	189
Sb	bdl	bdl	bdl				bdl	bdl	bdl	bdl	bdl	bdl	bdl			bdl	0.18	bdl	0.61	1.70	0.47		0.73	1.07
Sm	0.87	0.54	0.52				0.47	0.47	0.52	0.55	0.56	0.54	0.45			0.41	0.51	0.39	4.55	5.27	8.00		6.02	7.81
Sn	0.28	bdl	bdl				bdl	bdl	bdl	0.31	bdl	0.26	bdl			bdl	0.27	bdl	1.86	3.50	1.54		2.25	3.24
Sr	61	67	68				77	75	74	70	72	64	64			75	71	77	37	27	83		59	70
Ta	0.06	0.06	0.06				0.05	0.05	0.05	0.04	0.05	0.05	0.05			0.04	0.05	0.05	0.77	1.28	0.70		0.93	1.22
Tb	0.12	0.08	0.07				0.06	0.06	0.07	0.07	0.07	0.07	0.06			0.05	0.07	0.05	0.63	0.77	1.20		0.87	1.06
Th	0.76	0.65	0.63				0.57	0.57	0.75	0.70	0.58	0.58	0.64			0.57	0.73	0.57	8.6	14.2	7.5		11.2	15.3
Tm	0.06	0.04	0.04				0.03	0.03	0.04	0.03	0.04	0.04	0.03			0.03	0.03	0.02	0.33	0.49	0.55		0.43	0.52
U	0.72	0.68	0.71				0.73	0.72	0.77	0.76	0.78	0.76	0.60			0.75	0.77	1.15	2.9	4.2	4.9		4.2	5.8
V	9.0	4.7	5.0				6.0	5.9	8.4	9.6	6.8	8.5	10.7			9.6	10.1	6.1	123	147	98		132	185
W	bdl	bdl	bdl				bdl	bdl	bdl	bdl	bdl	bdl	bdl			bdl	bdl	bdl	1.1	1.8	1.6		1.3	2.0
Y	5.5	3.4	3.2				2.7	2.5	2.9	2.8	2.9	2.8	2.3			2.0	2.4	2.0	22	29	42		27	33
Yb	0.46	0.29	0.25				0.20	0.20	0.24	0.24	0.23	0.23	0.18			0.17	0.20	0.15	2.3	3.4	3.6		2.9	3.5
Zn	29	25	24				17	18	17	17	17	20	11			9.6	9.0	8.8	19	85	41		37	49
Zr	12.8	10.5	9.2				9.5	9.2	11.3	9.7	10.3	9.9	9.7			8.7	9.4	7.5	159	205	139		225	200
(all wt.%)																								
SiO_2	1.97	2.64	3.17				2.30	2.27	2.15	2.13	1.38	1.77	2.77			2.61	6.71	5.69	54.7	56.0	31.4		68.1	58.9
Al_2O_3	0.89	0.65	0.70				0.60	0.59	0.93	1.11	0.68	0.67	0.68			0.36	0.94	0.74	10.3	16.3	8.59		14.5	18.9
Fe_2O_3	2.85	2.03	2.16				1.54	1.55	1.60	1.55	1.70	1.88	1.87			1.64	1.71	1.38	2.75	8.34	4.47		3.95	5.59
MnO	0.179	0.101	0.091				0.08	0.08	0.085	0.081	0.086	0.097	0.102			0.089	0.084	0.075	0.06	0.013	0.318		0.015	0.019
MgO	18.0	18.5	18.4				18.8	18.9	18.7	18.7	18.9	18.9	18.8			19.2	18.3	18.8	5.83	2.51	10.4		1.67	2.43
CaO	29.7	29.9	29.7				30.0	30.2	30.0	29.9	30.3	30.3	29.7			29.9	28.0	28.5	7.51	1.25	15.3		0.34	0.41
Na_2O	bdl	bdl	bdl				bdl	bdl	bdl	bdl	bdl	bdl	bdl			bdl	bdl	bdl	0.26	0.87	0.18		0.29	0.22
K_2O	0.29	0.21	0.23				0.18	0.18	0.30	0.36	0.21	0.22	0.21			0.10	0.31	0.23	3.87	5.53	2.91		5.58	6.56
TiO_2	0.055	0.044	0.041				0.038	0.038	0.044	0.038	0.037	0.039	0.041			0.036	0.038	0.032	0.69	1.02	0.56		0.98	1.14
P_2O_5	0.041	0.026	0.033				0.035	0.035	0.048	0.055	0.045	0.042	0.043			0.03	0.038	0.042	0.11	0.17	0.13		0.12	0.15
LOI	44.5	45.0	44.2				44.9	45.1	45.0	45.0	45.4	45.0	44.9			45.1	42.8	43.8	13.6	7.8	25.2		4.1	6.3
Sum	98.5	99.1	98.7				98.5	98.9	98.9	98.9	98.8	98.9	99.1			99.1	98.9	99.3	99.7	99.7	99.4		99.6	100.6
% Clay	5.7	4.7	4.1				4.2	4.1	5.0	4.3	4.6	4.4	4.3			3.9	4.2	3.3	70.4	91.0	61.7		100	88.7

Abbreviations:

SARM - Le Service d'Analyse des Roches et des Minéraux du CNRS, Nancy, France

WHOI - Woods Hole Oceanographic Institution, U.S.A.

GR (Section) - Gayna River

CR (Section) - Cranswick River

SKR (Section) - Stone Knife River

S.D. - Standard Deviation (absolute value)

bdl - below detection limit

ID - isotope dilution

wt.% - percent by weight

% s.d. - percent standard deviation

cc - cubic centimeter

E2 - Thermo Electron Element 2 ICPMS

N - Thermo Fisher Neptune multicollector ICPMS

LOI - loss on ignition

Sum - sum of all major ions (listed as wt.%)

	SE 19	SE 20																							
1918	1988				2957	2958	2959	2986	2960	2987	2961	2988	2962	2963	2964	2965	2966	2989	2967	2969	2968	2970	2971	2990	2992
SKR					80705.01	80705.01	80705.01	80705.01	80705.01	80705.01	80705.01	80705.01	80705.01	80705.01	80705.01	80705.01	80705.01	80705.01	80705.01	80705.01	80705.01	80705.01	80705.01	80705.01	80705.01
N	N																								
duplicate	BIF	USGS-SDO-1	SRM values	S.D.	0-5	5-10	10-15	15-45	45-70	70-95	95-115	115-135	135-155	155-170	170-185	185-195	195-205	205-215	215-220	220-225	225-230	230-235	235-240	240-245	95-100
					9.71	15.72	13.25	10.02	10.01	10.32	10.09	9.96	10.06	9.98	10.14	9.58	10.18	13.07	10.38	9.88	9.79	10.58	9.42	11.50	10.04
0.8001	0.3299				0.9779	1.047	1.011	0.951	0.8874	0.8378	0.7987	0.7930	0.853	1.101	0.975	1.084	1.020	0.8948	0.908	0.8603	0.958	0.923	0.7746	0.8296	0.808
0.0023	0.0010				0.0030	0.006	0.004	0.005	0.0019	0.0031	0.0028	0.0023	0.003	0.011	0.005	0.007	0.005	0.0027	0.005	0.0031	0.014	0.004	0.0027	0.0018	0.005
540	25				7.7	5.0	7.3	10.1	13.9	23.9	18.8	20.0	13.4	7.1	7.1	6.3	12.0	17.8	11.3	16	10.6	9.7	17.0	17.9	19.7
0.2	3				11	11	9	6	6.4	2.6	4.8	3.2	6.6	12	12	14	7.3	2.7	7.6	5.7	8.4	8.5	5.6	3.1	3.2
104	6.0				6	5	6	10	11	16	11	6	7	6	5	10	12	6	13	21	7	9	6	7	11
3837	194				151	102	129	182	248	770	715	654	331	117	239	167	332	741	433	283	386	287	213	270	2088
1	10				7	19	7	6	7	9	3	8	5	10	6	8	10	6	10	15	11	11	16	9	9
2927	69				286	224	260	402	473	744	420	261	218	168	246	193	315	456	417	436	270	257	158	142	575
0	2				0.3	1	0.2	0.3	0.1	1	<0.1	1	0.2	1	0.3	0.2	1	1	1	1	1	1	4	0.2	<0.1
					41	85	1221	18	28	77		28	13	14	24	32	11	32	20	22	8	27	9	89	22
					15.14	49.04	477.3	5.06	5.68	9.03		3.90	2.73	5.68	9.64	14.7	2.63	5.07	5.02	3.85	2.14	7.87	1.47	13.9	3.12
					0.817	0.525	-4.06	0.897	0.827	0.742		0.751	0.824	1.04	0.872	0.928	0.992	0.841	0.855	0.819	0.935	0.839	0.759	0.681	0.774
	6.5	66.17	68.5	8.6																					
	13	350	397	38																					
	bdl	3.1	3.3	0.57																					
	bdl	0.33																							
	0.26	0.42																							
	5.2	68.3	79.3	7.8																					
	1.1	42.5	46.8	6.3																					
	30.2	68.2	66.4	7.6																					
	bdl	6.0	6.9	1.2																					
	bdl	55.5	60.2	9.6																					
	1.79	5.98	6	0.65																					
	1.40	3.30	3.6	0.55																					
	0.25	1.51	1.6	0.22																					
	1.01	16.8	16.8	1.8																					
	1.27	6.87	7.4	1.9																					
	1.69	1.58	1.3																						
	0.06	4.17	4.7	0.75																					
	0.44	1.17	1.2	0.11																					
	0.09	0.08	<2																						
	2.46	34.4	38.5	4.4																					
	0.24	0.49	0.54	0.14																					
	0.62	150	134	21																					
					35	31	37	46	63	100		93	88	143	187	188	190	207	313	182	94	140	96	126	182
	0.34	11.2	11.4	1.2																					
	3.71	33.5	36.6	3.3																					
	7.49	92.0	99.5	9.9																					
	bdl	28.9	27.9	5.2																					
	0.753	8.586																							
	0.5	116	126	3.9																					
	bdl	4.62	4.1-4.8																						
	0.83	7.13	7.7	0.81																					
	bdl	2.78	3.7	1.2																					
	24	71	75.1	11																					
	bdl	0.94	1.1	0.13																					
	0.22	1.02	1.2	0.24																					
	0.15	9.2	10.5	0.55																					
	0.21	0.49	0.45	0.08																					
	0.09	42	48.8	6.5																					
	49	155	160	21																					
	0.32	1.5	3.3																						
	17	38	40.6	6.5																					
	1.4	3.2	3.4	0.46																					
	bdl	62	64.1	6.9																					
	4.9	157	165	24																					
	26.8	47.8	49.3	0.63																					
	bdl	11.9	12.3	0.23																					
	69.9	9.19	9.34	0.21																					
	0.041	0.043	0.042	0.005																					
	0.015	1.50	1.54	0.038																					
	1.09	1.07	1.05	0.047																					
	bdl	0.35	0.38	0.026																					
	bdl	3.17	3.35	0.061																					
	0.03	0.68	0.71	0.031																					
	0.69	0.12	0.11	0.007																					
	0.7	24.3																							
	99.2	100.2																							

2993	2994	2995	2978	2979	2980	2972	2981	2982	2983	2984	2973	2991	2974	2985	3003	3004	3005	3006				
80705.01	80705.01	80705.01	81105.04	81105.04	81105.04	81105.04	81105.04	81105.04	81105.04	81105.04	81105.04	81105.04	81105.04	81105.04								
		N	N	N	N	N	N	N	N	N	N	N	N	N								
100-105	105-110	110-115	0-20	20-40	40-60	60-69	69-73	73-77	77-79	79-81	81-83	83-99	99-114	114-134	K-61	MJ-18	MJ-21	MJ-06	D-2.3	D-1.3	N-1.	N-2.
10.44	9.64	10.23	9.57	9.86	9.82	10.03	10.02	9.86	10.58	9.46	10.54	9.61	9.68	9.98	1.78	2.12	2.04	4.20				
0.884	0.6579	0.6663	0.947	0.7991	0.6797	0.7614	0.7000	0.839	0.7407	1.0098	1.0547	0.9102	1.016	0.894	0.561	1.958		2.290	0.976	0.868	0.864	0.919
0.005	0.0030	0.0025	0.004	0.0027	0.0019	0.0017	0.0021	0.005	0.0025	0.0016	0.0018	0.0017	0.005	0.005	0.007	0.013		0.030				
24.8	15.1	22.8	17.8	18.8	58.7	73.7	77.0	138	705	244	62.4	65.8	53.4	40.9	66	102		22	4	2	38	24
2.4	4.3	2.7	3.6	3.4	1.1	1.3	0.9	0.5	0.1	0.3	1.4	1	1.8	1.6	1.3	0.9		3.9				
14	8	5	2	1	3	9	7	20	84	115	31	20	13	5	44	35	42	19				
															1881	420		14				
3328	1739	1590	341		518	179	324	835	2873	2348	730	384	215	229								
15	9	8	19		10	7	9	5	2	3	10	9	5	13								
792	274	244	152	113	136	294	221	717	4085	1597	526	236	176	152		593	1751	487				
0.4	1	1	4	4	4	0.2	1	0.1	0.4	<0.1	1	1	0.5	3		2	5	19				
25	22	31	222	112	375	16	24	29	27	44	65	192	21	10787								
2.84	4.00	3.73	66.6	31.2	33	1.2	1.6	1.1	0.2	1.0	5.6	15.5	2.1	1399								
0.854	0.615	0.627	0.239	0.467	0.328	0.749	0.682	0.827	0.739	1.000	0.995	0.746	0.993	-14								
170	121	118	145	116	246	506	500	131	3345	3069	712	404	470	372								